1 **Multi-isotopic and trace element evidence against different formation pathways for oyster**

2 **microstructures**

3 *Niels J. de Winter[1,2]*, Linda K. Dämmer[3,4], Michaela Falkenroth[3,4,5], Gert-Jan Reichart[1,3], Simone Moretti[6],*

4 *Alfredo Martinez-García[6], Nils Höche[7], Bernd R. Schöne[7], Katerina Rodiouchkina[8], Steven Goderis[2], Frank*

5 *Vanhaecke[8], Martin Ziegler[1]*

6 [1]Dept. of Earth Sciences, Utrecht University, Utrecht, the Netherlands

7 [2]AMGC research group, Vrije Universiteit Brussel, Brussels, Belgium

8 [3]Ocean Systems Department, Royal Netherlands Institute for Sea Research and Utrecht University, Texel,

9 the Netherlands

10 [4]Environmental Geology, Department of Geology, Institute of Geosciences, University of Bonn, Bonn,

11 Germany

12 [5]Neotectonics and Natural Hazards Research Group, Rheinisch-Westfälische Technische Hochschule

13 Aachen, Aachen, Germany

14 [6]Max Planck Institute for Chemistry, Otto Hahn Institute, Mainz, Germany

15 [7]Institute of Geosciences, University of Mainz, Mainz, Germany

16 [8] Atomic and Mass Spectrometry - A&MS research group, Department of Chemistry, Ghent University,

17 Ghent, Belgium

18

19   **Abstract**

20   Shells of oysters (Ostreidae) are predominantly composed of foliated and chalky calcite microstructures.

21   The formation process of the more porous chalky structure is subject to debate, with some studies

22   suggesting that it is not formed directly by the oyster but rather through microbial mineralization within the

23   shell. Here, this hypothesis is tested in modern shells of the Pacific oyster (*Crassostrea gigas*) from coastal

24   regions in France and the Netherlands. We compare measurements of stable carbon, oxygen, nitrogen,

25   sulfur and clumped isotope ratios with high resolution spatially resolved element (Na, Mg, Cl, S, Mn and Sr)

26   data and microscopic observations of chalky and foliated microstructures in the oyster shells. Our results

27   barely resolvable to no isotopic differences between the different microstructures, arguing against formation

28   of the chalky calcite by microorganisms. However, we observe a small difference in the oxygen isotope

29   ratio (0.32‰) and clumped isotope composition (0.017‰) between the microstructures, which is caused by

30   the fact that growth of the chalky microstructure is more biased towards warmer months. This bias can be

31   avoided by sampling the foliated microstructure only. The strong seasonal variability recorded in the shell

32   should also be considered in reconstructions of mean annual temperatures. Significant differences in

33   element concentrations were found between the two microstructures. A combination of Na, Mg, Cl, S, Mn

34   and Sr profiles, recorded with high (25-50 μm) lateral resolution, with sub-annual age models and *in situ*

35   observations of variability in temperature and salinity allows us to estimate distribution coefficients between

36   seawater and shell calcite for these elements. The results show that only Sr is incorporated into the shell

37   of *Crassostrea gigas* in near-equilibrium with seawater. A significant difference is found between the

38   distribution coefficients for incorporation of Na, Mg, Cl and S into the foliated and chalky microstructures

39   respectively, independent from environmental conditions but correlating with differences in mineralization

40   rate. As mineralization rate affects element incorporation into oyster shells, potential element proxies for

41   paleoclimate reconstructions should take growth rate effects into account, and relationships between

42   mineralization rate and element concentrations should be studied before such proxies can be applied with

43   confidence.

44

45   **1. Introduction**

46   Oysters (Ostreidae) are a highly diverse and specialized group of bivalves that live cemented to hard

47   substrates, predominantly in shallow marine environments (Yonge, 1960). Oysters have obtained a

48   widespread distribution and inhabit a diverse set of environments, from fully marine habitats to turbid

49   brackish estuaries (Carriker, 1951; Huber, 2010; Do Amaral and Simone, 2014). As reef builders, many

50   oyster taxa are keystone species in shallow marine environments (Newell, 1988; Grabowski and Peterson,

51   2007; Scyphers et al., 2011; Grabowski et al., 2012). Furthermore, oyster reefs play a vital role in local

52   chemical cycles due to their high population density and highly efficient filtration (Dame et al., 1984; Dame,

53   1999; zu Ermgassen et al., 2013). The formation, structure and chemistry of oyster shells is of interest

54   because their composite shell structures have attractive (mechanical) properties which have various

55   industrial applications (Addadi et al., 2006; Cranford and Buehler, 2010; Luz and Mano, 2010) and because

56   oyster shells serve as high-resolution archives for past climates and environments (Surge and Lohmann,

57   2008; Ullmann et al., 2010; Mouchi et al., 2013; Bougeois et al., 2018; de Winter et al., 2018; 2020).

58   Many oysters grow thick, irregular shells predominantly consisting of two different calcite microstructures.

59   The "foliated" calcite consists of densely packed, foliated calcite laths while the "chalky" calcite (Gray, 1833)

60   is composed of more loosely and chaotically organized blades surrounded by interconnected pores

61   (Carriker et al., 1980; Checa et al., 2007). Other mineralized structures include smaller volumes of prismatic

62   calcite on the adductor muscle scar and shell margins (e.g., in *Crassostrea virginica*) and minor amounts

63   of aragonite fortifying the resilium (Carriker et al., 1980). The presence of the chalky structure in the form

64   of lenses between the foliated calcite is unique to the Ostreidae family and its process of formation is highly

65   debated. This has recently spurred researchers to investigate the chemical (Surge et al., 2001; Ullmann et

66   al., 2010; 2013), microstructural (Lee et al., 2011; Checa et al., 2018; Banker and Sumner, 2020) and

67   physiological (Higuera-Ruiz and Elorza, 2009) differences between chalky and foliated structures. Some

68   authors suggest that the chalky structure may be formed through "remote mineralization" by sulfur-reducing

69   bacteria living within shell vesicles (Chinzei and Seilacher, 1993; Vermeij, 2014). Others, however, have

70   challenged this hypothesis by suggesting the structural difference results from local detachment of the

71   mantle from the forming shell. This would serve as a mechanism to accommodate the typical plasticity of

72   shell shape allowing oysters to attach to rough substrates and adapt to space limitations during growth

73   (Checa et al., 2018; Banker and Sumner, 2020). This distinction has important implications both for

74 understanding the formation pathway of these biomineralized structures and for the interpretation of the

75 chemistry of oyster shell calcite for environmental monitoring and paleoclimate reconstruction.

76 While some authors have reported chemical and isotopic differences between oyster microstructures, for

77 example, in their elemental composition (e.g. Higuera-Ruiz and Elorza, 2009; Ullmann et al., 2010; 2013),

78 the origin of these differences is poorly understood because these studies lack characterization of the

79 differences in key isotopic systems (e.g. nitrogen and sulfur isotope ratios) or a precise link between shell

80 chemistry and *in situ* measurements of the growth environment. The strong isotopic fractionation associated

81 with microbial sulfur reduction (Brunner et al., 2005; Jia et al., 2014) and the large differences in element

82 partitioning between eukaryotic and microbial carbonates (e.g. McGenity and Sellwood, 1999; Webb and

83 Kamber, 2000; Terakado et al., 2000) may provide conclusive evidence for or against the "remote

84 mineralization" hypothesis in the chemical and isotopic signatures of the respective microstructures.

85 Here, we combine multiple stable isotope ratio ($\delta^{13}C_c$, $\delta^{15}N$ and $\delta^{34}S$) analyses from both chalky and foliated

86 microstructures in the Pacific oyster *Crassostrea gigas* (Thunberg, 1793; syn. *Magallana gigas*) with *in situ*

87 trace element records to test the "remote mineralization" hypothesis in modern oysters. In addition to this

88 multi-proxy dataset, we present stable oxygen ($\delta^{18}O_c$) and clumped isotope (Δ_{47}) values of the carbonate

89 in the microstructures. As common proxies for paleotemperature, we assess whether $\delta^{18}O_c$ and Δ_{47} values

90 in both microstructures reliably record the temperature and isotopic composition of the seawater ($\delta^{18}O_{sw}$)

91 and could be used for climate reconstructions. Finally, we evaluate the distribution coefficients of Na, Mg,

92 Cl, S, Mn and Sr into the chalky and foliated microstructure of *C. gigas*, shedding new light on the chemical

93 differences between the microstructures and the potential use of element records for environmental

94 reconstructions.

95

96 **2. Materials and Methods**

97 2.1 Sample acquisition

98 A total of 18 specimens of *C. gigas* were collected from three different localities (see **Fig. 1**). Eight

99 specimens (hereafter: **O1-8**) were obtained from a cultivation area in coastal Brittany (France, 49°04.00' N,

100   001°35.47' W; hereafter "BR") where they were grown at an average water depth of 5-10 meters. The

101   bivalves were harvested on February 14th, 2017. Six specimens were collected in the Mokbaai, a tidal inlet

102   located in the protected National Park Duinen van Texel at the southern coast of the island Texel in the

103   Wadden Sea in the northwest of the Netherlands (53°00.90' N, 004°45.20' W, hereafter "MB"). Two of these

104   specimens (hereafter: **M1** and **M2**) were collected during a first sampling campaign on July 6th, 2017 and

105   four additional specimens (**M3-6**) were collected during a second campaign on July 5th, 2018. Four

106   specimens were collected from the harbor of the TESO ferry at the southern coast of Texel (53°00.10' N,

107   004°46.20' W, hereafter "TH"). Two of these specimens (hereafter: **H1** and **H2**) were collected during a first

108   sampling campaign on July 6th, 2017 and two additional specimens (**H3** and **H4**) were collected during a

109   second campaign on July 5th, 2018.

110
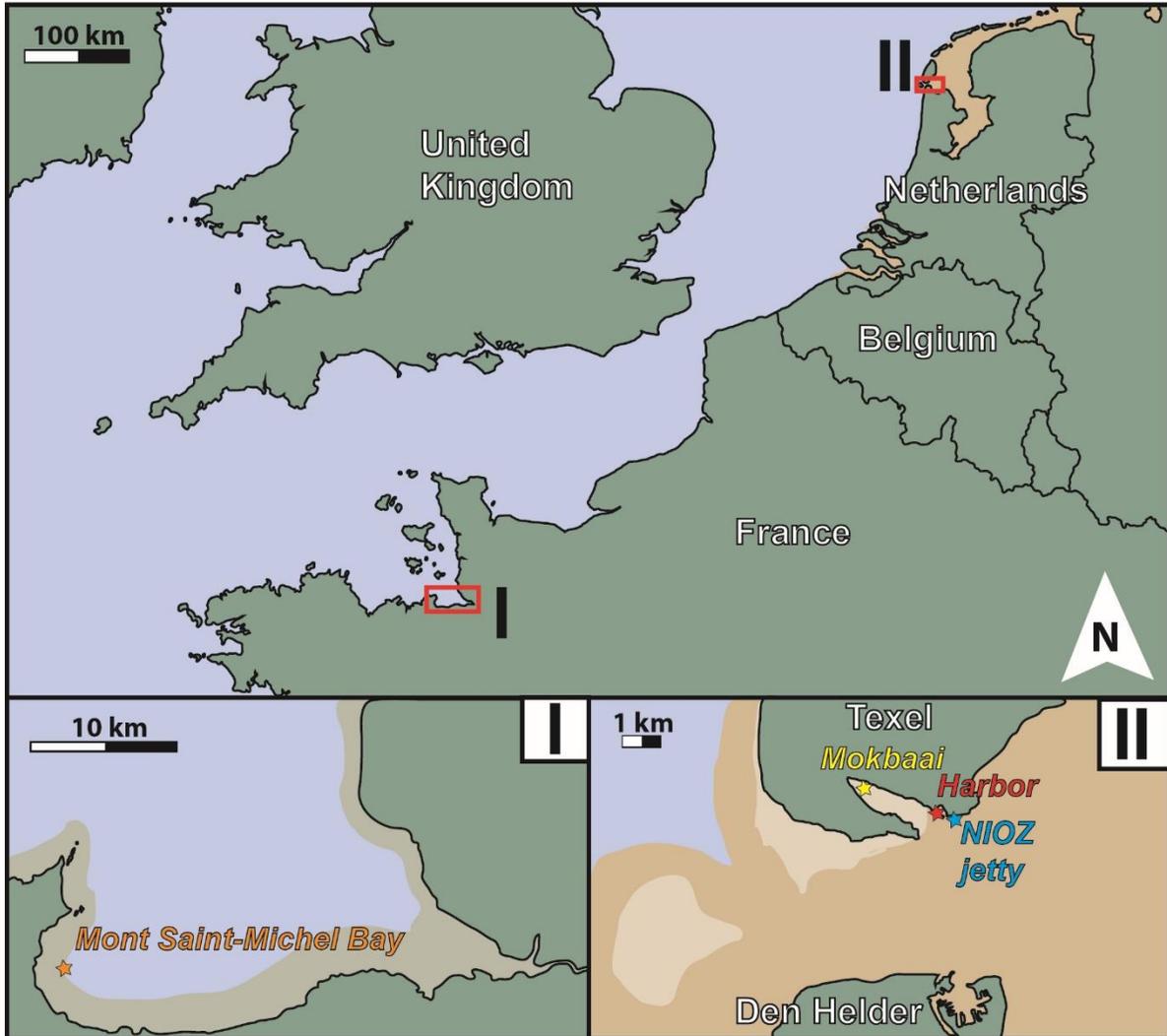
Figure 1: *Overview of the three localities where the specimens of* C. gigas *used in this study were acquired. Star-shaped symbols highlight the sampling sites of specimens **O1-8** from Brittany (France, in orange), **M1-6** from the Mokbaai (NL, in yellow) and **H1-4** from TESO Harbor (NL, in red). The jetty of NIOZ where in situ sea surface temperature and salinity measurements were done is indicated in blue. Light brown colors indicate parts of the tidal estuary that fall dry during low tide.*

2.2 Sample preparation

The convex left valves of the shells were superficially cleaned to remove algae and other contaminants using a soft brush and an ultrasonic bath. They were disinfected using acetone (C_3H_5OH) and distilled water, and oven dried overnight at 50°C. Left valves were chosen in this study because they are larger,

120   contain relatively low amounts of aragonite in oysters, and have better developed hinges (see Kennedy et

121   al., 1996; Surge et al., 2001). This provides more surface area for measurement, allows growth features to

122   be more readily recognized and permits a higher sampling resolution. Shell valves were sectioned

123   dorsoventrally along their axis of maximum growth (following Surge et al., 2001) using a slow rotating saw

124   with a diamond coated blade (thickness = 1 mm). From the larger shells from Texel (**M1-4**, **H1-4**), the hinge

125   plate was removed for easier handling. The cross-sections of all samples were polished using silicon

126   carbide polishing disks (up to P2400 grit size). Polished samples were imaged by means of color scanning

127   (RGB) using an Epson® 1850 flatbed scanner (Seiko Epson Corp., Nagano, Japan) at a pixel resolution of

128   6400 dpi (± 4 µm pixel size; see **Fig. 2**). The opposing sides of the cross-section through the shell hinge of

129   selected specimens (**O2**, **O6**, **O7**, **O8, M2**, **M5** and **H1**) were cut parallel to the growth axis and mounted

130   on glass slides to produce thick sections for microscopy. These thick sections were polished using a 1.00,

131   0.30 and 0.05 µm Al_2O_3 suspension. Polished thick sections were treated with Mutvei's solution, a reagent

132   that etches the surface, fixes organic compounds and stains mucopolysaccharides, which aids in identifying

133   microgrowth patterns (Schöne et al., 2005a). The sections were immersed in Mutvei's solution which was

134   held at 38°C for 20 minutes under constant stirring until properly stained.
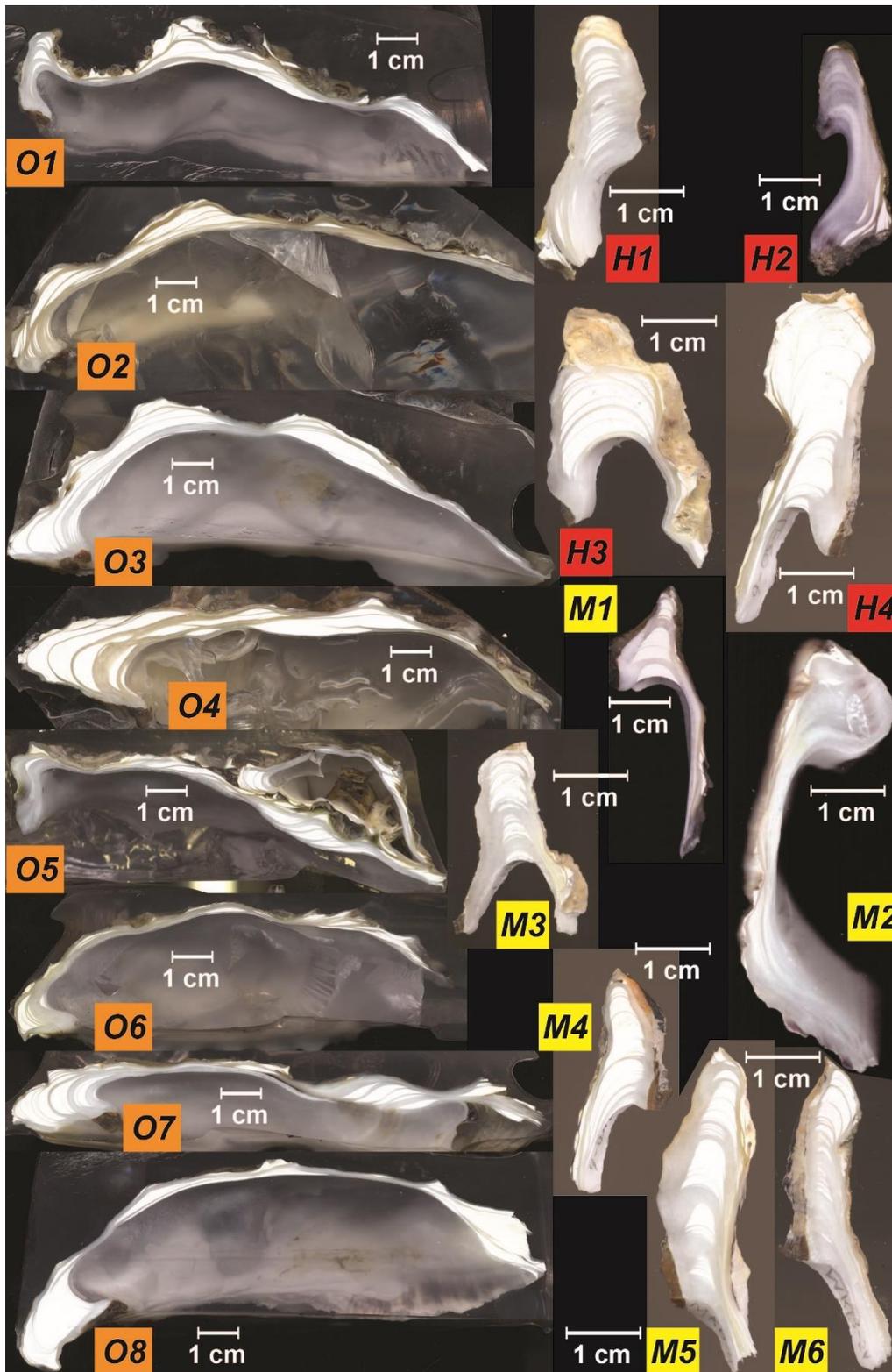
Figure 2: Overview of color scans taken of cross-sections through the entire shell (**O1-8**, in orange) or hinge region (**H1-4**, in red, and **M1-6**, in yellow).

138   2.3 Microscopy

139   Polished thick sections were imaged both before and after Mutvei staining using a stereomicroscope with

140   sectoral dark field illumination at 30× magnification. Images were taken covering the full polished surface

141   of the hinge using a Canon EOS 550D camera and stitched together into a microscopic composite using

142   the image processing software ImageJ/Fiji (Schindelin et al., 2012; see reduced-quality versions in **Fig. 3A-**

143   **B** and full quality versions in **S1**). Thick sections of specimens **O2**, **O6** and **O7** were then mounted on a

144   Scanning Electron Microscope (SEM) stub with adhesive carbon stickers and sputtered with a 4-5 nm thick

145   platinum layer. Images were taken using a LOT Quantum Design Phenom PRO Desktop SEM (Quantum

146   Design GmbH, Grimbergen, Belgium; third generation) equipped with a $CeBr_6$ source and backscatter

147   electron detector operating at a voltage of 10 kV and a working distance of ca. 2 mm (following Höche et

148   al., 2020). SEM magnifications varied between 200× and 16000×. Full quality versions of SEM micrographs

149   are provided in **S1**.
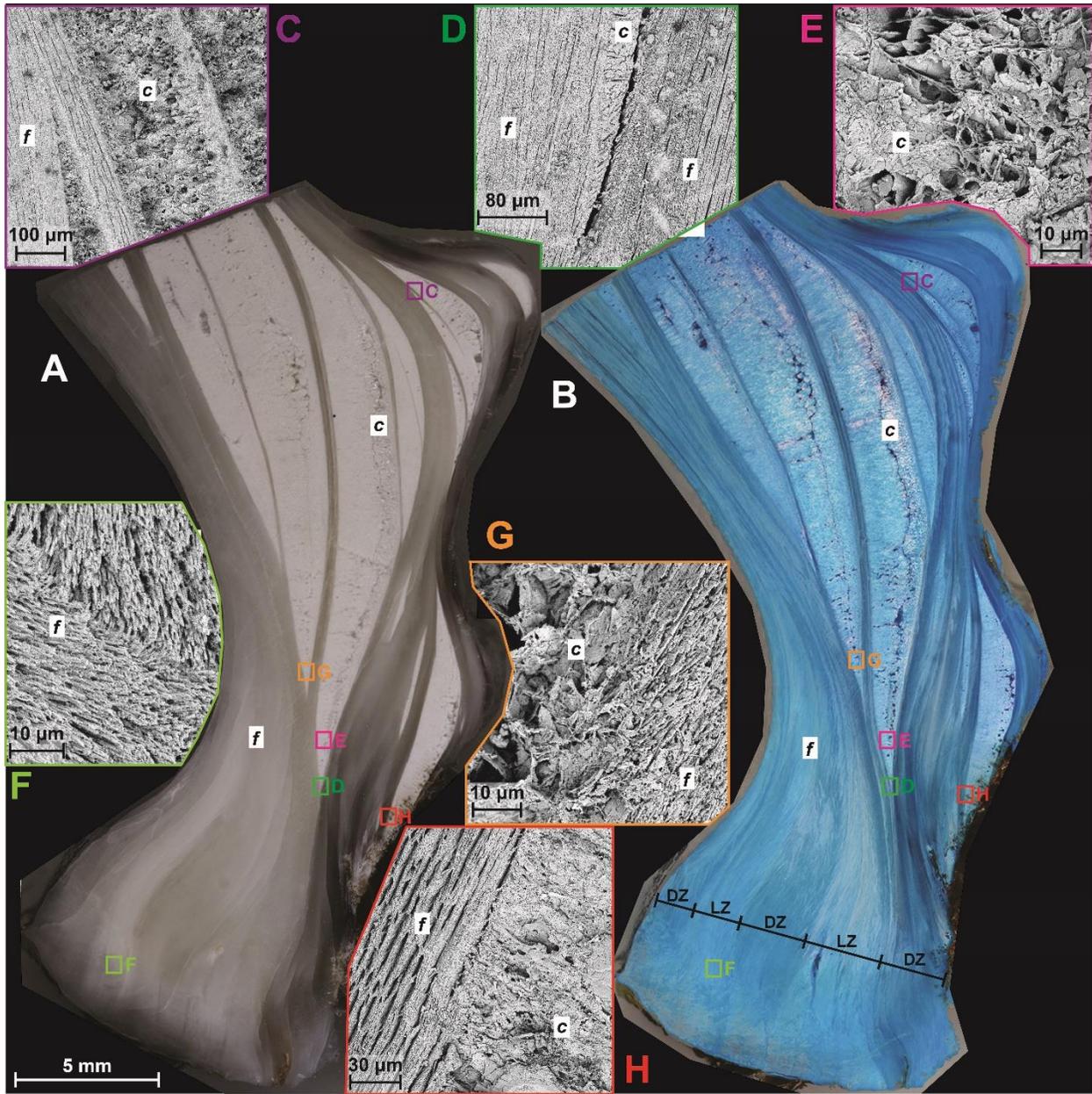
Figure 3: *Compilation of microscopic images of the two microstructures in the hinge region of* C. gigas. *In all images, "f" denotes occurrence of the foliated microstructure while "c" indicates where the chalky structure is exposed. **A)** Composite of reflected light microscopy images of the hinge region of sample **O2** before Mutvei staining (opposite side of the cross-section shown in **Fig. 2**). **B)** Composite of reflected light microscopy images of the hinge region of sample **O2** after Mutvei staining, with "DZ" and "LZ" indicating the occurrence of dark and light bands in the foliated microstructure (sensu Higuera-Ruiz and Elorza, 2009) **C)** SEM close-up image of a region where the edge of a lens of chalky structure is visible between foliated*

158 *calcite layers. **D)** SEM close-up of the tip of a lens of chalky structure, which tapers off in between foliated*

159 *laminae. Note how foliated laths on the right side (dorsal side, deposited before the chalky structure) of the*

160 *lens change orientation towards the chalky structure and transition into the chalky microstructure. **E)** SEM*

161 *close-up of chalky microstructure showing the irregular orientation of calcite blades and the large*

162 *interconnected pore space in between. **F)** SEM close-up of the foliated microstructure showing densely*

163 *packed calcite folia with changes in mineral orientation, which become more common close to the outer*

164 *margin of the hinge (bottom of **A** and **B**). **G)** SEM close-up of the transition from foliated (right, or dorsal*

165 *side, deposited first) to chalky (left, or ventral side, deposited second) calcite showing how the foliated*

166 *calcite laths smoothly transition into the chalky microstructure by changing their orientation and loosening*

167 *their packing. **H)** SEM close-up of chalky microstructure (right, dorsal side) transitioning into foliated*

168 *microstructure (left, ventral side, deposited after chalky microstructure). Note how the oldest foliated laths*

169 *on the bottom of the image (in direction of the hinge) taper out into the chalky structure while folia deposited*

170 *afterwards (farther to the left, or ventral, side) continue further. Note also that the folia are initially less*

171 *densely packed, organized in bundles, and regain their typical structure later (compared with **D** and **F**). Full*

172 *size SEM images are provided in **S1**.*

173 2.4 X-ray fluorescence spectrometry

174 Elemental concentrations were measured *in situ* in the hinge region on the polished cross-sections using a

175 Bruker® M4 Tornado micro-X-ray Fluorescence scanner (Bruker nano GmbH, Berlin, Germany) equipped

176 with a Rh X-Ray source using maximum energy settings (50 kV, 600 µA) with a spot size of 25 µm (Mo Kα)

177 and two Silicon Drift detectors. The XRF setup is described in detail in de Winter and Claeys (2017).

178 Quantitative XRF element profiles were obtained for all polished cross-sections using two measurement

179 strategies (see **Fig. 4**): First, a profile was measured in the direction of maximum growth through the hinge

180 of the shell in cross section, perpendicular to the growth bands and crossing foliated and chalky calcite

181 layers (as in Surge et al., 2001; Ullmann et al., 2010; 2013). Second, a profile was measured perpendicular

182 to the growth lines, exclusively sampling the dense foliated calcite layers in the hinge of the shell (as in

183 Surge and Lohmann, 2008; Mouchi et al., 2013; Durham et al., 2017). The position of the profiles is

184 indicated in **S2**. All element profiles were measured using the point-by-point line scanning method outlined

185 in de Winter et al. (2017a). An integration time of 60 s per point and the sampling density (20-40

186 analyses/mm, variable between individuals) were chosen as a compromise between obtaining high-

187 resolution profiles and achieving sufficient count statistics for the instrument to reach the Time of Stable

188 Reproducibility (TSR) in order to provide reproducible concentrations for the elements of interest (de Winter

189 et al., 2017b). All XRF line scans were quantified using the Bruker Esprit® fundamental parameters (FP)

190 quantification relative to the BAS CRM 393 limestone standard (Bureau of Analyzed Samples,

191 Middlesbrough, UK; BAS) and calibrated using a range of certified carbonate reference materials: CCH-1

192 (Université de Liège, Belgium), COQ-1 (US Geological Survey, Denver, CO, USA), CRM393 (BAS),

193 CRM512 (BAS), CRM513 (BAS), ECRM782 (BAS) and SRM-1d (National Institute of Standards and

194 Technology, Gaithersburg, MD, USA). R^2 values of calibration curves exceeded 0.99 and reproducibility

195 standard deviations were better than 10 % relative to the mean. For the purpose of this study, the discussion

196 of element profiles is limited to the concentrations of sodium (Na), magnesium (Mg), sulfur (S), chlorine

197 (Cl), calcium (Ca), manganese (Mn) and strontium (Sr). Raw data of µXRF analyses is provided in **S3** and

198 **S4**.

199
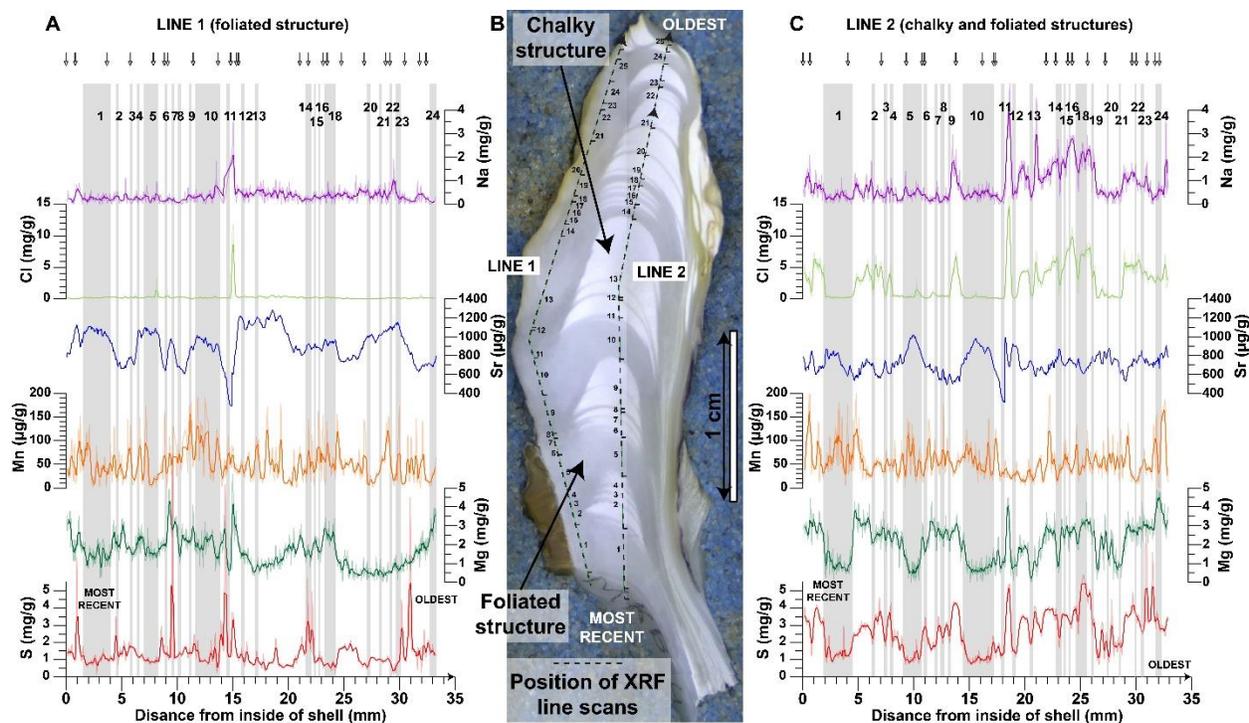
200 **Figure 4**: *Examples of high-resolution X-Ray Fluorescence profiles through the hinge of specimen **M5**.*

201 *Profiles are plotted from the inner (bottom in image **B**) to the outer surface (top in image **B**) of the shell, or:*

202 *from most recently formed to oldest shell material (see dashed arrows in **B**). Plots **A** and **C** show*

203 *concentrations of (from top to bottom) Na (purple), Cl (light green), Sr (dark blue), Mn (orange), Mg (dark*

204 *green) and S (red) in profiles exclusively through the foliated structure (line 1; **A**) and through both structures*

205 *(line 2, **B**) respectively. Arrows above these plots indicate the locations of tick marks on the dashed arrows*

206 *in **B**, while numbers below the arrows count the number of foliated layers in line 2 (**C**) and their*

207 *contemporary locations in line 1 (**A**). Both were used to temporally align parts of the profiles that represent*

208 *shell material that formed simultaneously.*

209 2.5 Age model

210 In previous studies, microgrowth increments were often used to assess the timing and growth rate of bivalve

211 shell carbonate (e.g. Jones, 1983; Schöne et al., 2005b). However, some bivalve species mineralize shells

212 without clear microgrowth patterns (such as those of *C. gigas*; Huyghe et al., 2019). In these cases,

213 alternative techniques are developed to estimate seasonally varying growth rates and reconstruct the timing

214 of shell growth based on the strong relationship between $\delta^{18}O_c$ and temperature seasonality (e.g. Wilkinson

215 and Ivany, 2002; Goodwin et al., 2003; 2009; Judd et al., 2018). Due to the complexity added by variations

216 of seasonal growth rate and environmental parameters, building accurate intra-annual chronologies

217 requires high-resolution $\delta^{18}O_c$ data (>20 samples/year; Goodwin et al., 2003). This makes it ineffective in

218 terms of costs and time for studies targeting larger numbers (>10) of specimens, such as this one.

219 Fortunately, recent studies have shown that Mg/Ca ratios in oyster shells follow the seasonal temperature

220 cycle (Surge and Lohmann, 2008; Ullmann et al., 2013; Mouchi et al., 2013), and that annual cycle counts

221 in Mg/Ca profiles yield accurate, reproducible estimates of shell ages (Durham et al., 2017). The consistent

222 correlation between Mg/Ca and temperature seasonality is also clear in specimens **H1**, **M1** and **M2** for

223 which inter-annual $\delta^{18}O_c$ profiles were measured (see **2.9** and **S5**). Since Mg/Ca profiles can be analyzed

224 efficiently at high resolution, we adapted an age modeling routine which estimates seasonally changing

225 growth rates and the timing of shell formation in bivalves from $\delta^{18}O_c$ profiles by (Judd et al., 2018) in Matlab

226 (Mathworks, Nantick, MA, USA; script given in **S6**) to work with high-resolution µXRF Mg/Ca data (see **2.4**).

227 Mg/Ca profiles were smoothed using a moving average and normalized before applying the modelling

228 routine (following Durham et al., 2017). In order to prevent bias on Mg concentrations introduced by

229 microstructural change, age models were based solely on Mg/Ca profiles that were measured entirely in

230 the foliated microstructure. A date relative to the annual cycle was assigned to each µXRF measurement

231 point by combining growth rate and temperature sinusoids to simulate the Mg/Ca curve until an optimal fit

232 with the data was achieved (see Judd et al., 2018). The age model was then projected on µXRF lines

233 through both microstructures using the position of the line scans in combination with microscopic growth

234 increments observable on color scans (see **Fig. 4**). Relative timing of both µXRF profiles was validated by

235 comparing their Sr/Ca profiles, which are unaffected by microstructural change (see **3.2**). Ages of shell

236 portions were converted to calendar dates by anchoring the youngest portions of the shell to the harvest

237 date of the specimen. Results of age modelling are provided in **S7**.

238 2.6 Ambient sea water conditions

239 High-resolution (hourly) time series of sea surface temperature (SST) and sea surface salinity (SSS) were

240 measured *in situ* on the jetty of the Netherlands Institute for Sea Research (NIOZ) located on the southern

241 coast of the island of Texel (53°0.1' N latitude and 4°47.3' W longitude) within 5 kilometers from the sample

242 location for the Mokbaai and TESO harbor samples (**M1-6** and **H1-4**; see **Fig. 1**). Data from the NIOZ jetty

243 for the period from 2001 up to and including 2018 was supplied by Eric Wagemaakers and Sonja van

244 Leeuwen (pers. comm.; **S8**). This location experienced a seasonal SST range of 3-21°C (based on daily

245 averages, the monthly average SST range is 3-19 °C; see **S8**) with a mean annual average of 11°C and

246 daily SSS range of 25-32 psu (based on daily averages, the monthly average SSS range is 26.6-29.1 psu;

247 see **S8**) around an annual mean of 28 psu. SST and SSS time series for the French locality were obtained

248 from a compilation of *in situ* SST and SSS measurements from local stations, data from which were

249 obtained from the Institut Français de Recherche pour l'Exploitation de la Mer (IFREMER, Issy-les-

250 Moulineaux, France; http://www.ifremer.fr/co-en/, last access 18/05/2020 see **S9**). The sampling location

251 on the Brittany coast experienced a seasonal SST range of 5-21°C with a mean annual average of 13.6°C

252 and an SSS range of 32-35 around an annual mean of 33. In absence of *in situ* sea water $\delta^{18}O_{sw}$ and

253 elemental (Na, Mg, S, Cl, Ca, Mn and Sr) concentrations, sea water elemental and $\delta^{18}O$ composition was

254   calculated assuming conservative behavior of these elements in sea water and mixing with freshwater of

255   negligible element concentrations and a $\delta^{18}O_{sw}$ of -7.9‰VSMOW (Mook, 1970; Quinby and Turehian, 1983;

256   Pilson, 2012; IAEA, 2015; van Hulten et al., 2016; Bowen, 2020; details in **S10**)

257   2.7 Calculation of element distribution coefficients

258   Distribution coefficients (D) for the elements Na, Mg, Cl, S, Mn and Sr between calcite of the foliated and

259   chalky microstructures and seawater were calculated from concentrations in these microstructures and

260   concentrations of the respective elements in seawater at the time of shell formation using the following

261   equation:

262
$$D_X = \frac{[X]_{carbonate}/[Ca]_{carbonate}}{[X]_{seawater}/[Ca]_{seawater}}$$

263   Here, X is the element in question and D_x is the distribution coefficient of that element between water and

264   shell calcite of the respective microstructure. A date of shell formation was assigned to each µXRF data

265   point to match each data point to a local SSS measurement and associated seawater composition (see

266   **2.7**). Detailed documentation of the position of these µXRF profiles allowed each data point to be placed

267   either within the foliated or chalky microstructure (see **Fig. 4**). As a result, seasonally weighted averaged

268   distribution coefficients for both microstructures could be calculated for a specimen by averaging the

269   distribution coefficients calculated individually for each data point within one microstructure or the other.

270   This procedure was carried out for specimens **O1-8**, **M4-6** and **H4**. Uncertainties on distribution coefficients

271   were calculated from variability within microstructures in each specimen. These uncertainties include

272   uncertainties on dating and alignment of the microstructures using the age model. Elemental distribution

273   coefficients for both microstructures in all specimens are provided in **S11**. Response of distribution

274   coefficients to seasonal variability in the environment was investigated using sinusoidal regression (see

275   **S10**)

276   2.8 Carbon and oxygen isotopic analysis

277   Small (20-45 µg) aliquots of calcite were drilled from the hinges of specimens **H1**, **M1** and **M2** in the direction

278   of the axis of maximum growth using a high-precision, computer-driven Micromill (New Wave Research)

279   attached to an x, y and z stage following digitized milling path positions. Calcite carbon ($\delta^{13}C_c$) and oxygen

280   ($\delta^{18}O_c$) isotope values were measured using an automated carbonate device (Thermo-Kiel 105 IV)

281   connected to a Thermo Finnigan MAT 253 Dual Inlet Isotope Ratio Mass Spectrometer (IRMS) at the Royal

282   Netherlands Institute for Sea Research (NIOZ). NBS-19 limestone was used as standard material for the

283   calibration, while the Vrije Universiteit Internal Carbonate Standard (VICS: $\delta^{18}O_c$ = -5.44 ‰; $\delta^{13}C_c$ = 1.35

284   ‰; Pracht et al., 2018) was measured after every seventh sample and used for drift detection and

285   correction. External precision of the NBS-19 standard measurements was always better than 0.1‰ for both

286    $\delta^{18}O_c$ and $\delta^{13}C_c$. All stable isotope ratio results are provided in **S11**.

287   2.9 Carbonate clumped isotope analysis

288   Larger calcite samples (~15 mg) were drilled from both the foliated and chalky microstructure of specimens

289   **M2** and **M6** for clumped isotope analyses using a handheld Dremel 3000 (Robert Bosch GmbH, Racine,

290   WI, USA) rotary drill equipped with a tungsten carbide drill bit (Ø = 1 mm). An excess amount of sampling

291   of both microstructures was done along multiple growth years in the hinge of the specimens to ensure

292   proper mixing of seasonal variability. Several ~90 μm aliquots from the foliated (23 aliquots) and chalky (23

293   aliquots) structure of **M2** and the foliated (18 aliquots) and chalky (19 aliquots) of **M6** were analyzed using

294   a Thermo Fisher Scientific MAT253 PLUS mass spectrometer coupled to a Kiel IV carbonate preparation

295   device. Aliquots were reacted at 70 °C with nominally anhydrous (103 %) phosphoric acid. The resulting

296   CO_2 gas was cleaned from water and organic compounds with two cryogenic liquid N_2 traps and a PoraPak

297   Q trap kept at -40 °C. The purified sample gases were analyzed in micro-volume LIDI mode with 400 s

298   integration time against a clean CO_2 working gas ($\delta^{13}C_c$ = -2.82 ‰VPDB; $\delta^{18}O_c$ = -4.67 ‰VPDB; Δ_{47} = 0

299   ‰VPDB), corrected for the pressure baseline (Bernasconi et al., 2013; Meckler et al., 2014) and converted

300   into the absolute reference frame by computing an empirical transfer function from ETH calcite standards

301   (ETH-1, -2, -3) analyzed on different days and their accepted values (Bernasconi et al., 2018; Kocken et

302   al., 2019). Sample data were corrected for background drift by bracketing with ETH-3 standard aliquots. All

303   isotope ratio data were calculated using the new IUPAC parameters following Daëron et al. (2016) and Δ_{47}

304   values were projected to a 25 °C acid reaction temperature with a correction factor of 0.062 ‰ (after

305   Defliese et al., 2015 and Murray et al., 2016). Long-term Δ_{47} reproducibility standard deviation was

306   determined to be 0.04‰ based on repeated measurements of ~90 µg aliquots of our control standard IAEA

307   C2 (Δ_{47} of 0.719‰; measured over a 20-month period; see **S12**). Calcification temperatures were calculated

308   from Δ_{47} values using the temperature calibration by Kele et al. (2015) modified by Bernasconi et al. (2018).

309   For the $\delta^{18}O_c$ values, we applied an acid correction factor of 1.00871 (Kim and O'Neil, 1997). Both $\delta^{18}O_c$

310   and $\delta^{13}C_c$ were reported versus VPDB with a typical reproducibility below 0.08‰ and 0.04‰, respectively

311   (95 % confidence level). To calculate the $\delta^{18}O_{sw}$ from Δ_{47} and $\delta^{18}O_c$, we used the $\delta^{18}O_c$-temperature

312   relationship of Kim and O'Neil (1997). Only $\delta^{18}O_c$ values from aliquots used for Δ_{47} measurements were

313   used to calculate $\delta^{18}O_{sw}$. The number of Δ_{47} aliquots per sample enabled temperature estimates from Δ_{47}

314   in foliated and chalky microstructures with an error of ± 3.3°C (95 % confidence level). Raw data and

315   metadata associated with all clumped isotope analyses are provided in **S12**.

316   2.10 Nitrogen isotopic analysis

317   We determined nitrogen isotope ratios ($\delta^{15}N$) of organic matter bound to calcite in the foliated and chalky

318   microstructures of specimens **M2**, **M6**, **H2** and **H3** on the same samples used for carbonate clumped

319   isotope analyses (see details in **S10**). Briefly, calcite samples were subjected to reductive and oxidative

320   cleaning. After cleaning, samples were dissolved in acid, and fossil-bound organic N was oxidized to nitrate

321   using a basic solution of potassium peroxydisulfate ($K_2S_2O_8$) following the protocols previously described

322   for other fossil types (e.g. foraminifera, corals and otoliths; Ren et al 2009; Straub et al 2013; Wang et al

323   2014; 2016; Lueders-Dumont 2018). The isotopic composition and N content were measured using the

324   'denitrifier method', in which nitrate is quantitatively converted to nitrous oxide (N_2O) by denitrifying bacteria

325   (Sigman et al., 2001; Weigand et al., 2016). The external precision of our $\delta^{15}N$ results across multiple

326   batches analyzed was 0.20‰, based on the measurement of in-house coral standards.

327   2.11 Sulfur isotopic analysis

328   The isotopic composition ($\delta^{34}S$) of carbonate-associated sulfur in the foliated and chalky structure of

329   specimens **H2** and **H3** was measured using a multi-collector - inductively coupled plasma - mass

330   spectrometer (MC-ICP-MS; Neptune XT, Thermo Fisher Scientific, Bremen, Germany). Our instrumental

331   setup and sample preparation are based on methodology detailed in Paris et al. (2013). Details on sample

332   preparation, instrumental setup and data treatment are reported in **S10**. Due to the large (100–160 mg)

333   sample size required for the δ³⁴S analyses, the number of full replicates per microstructure within shells

334   was limited and multiple digestions for each sample were not possible to estimate the uncertainty of the

335   whole procedure. The expanded uncertainty (95% confidence level) of δ³⁴S measurements on individual

336   samples was determined to be 0.55‰ by using the mean standard deviation from two carbonate non-

337   isotopic certified reference materials (BAS ECRM782-1 dolomite; Bureau of Analysed Samples Ltd.,

338   Middlesbrough, UK and NIST-1d limestone; National Institute of Standards and Technology, Gaithersburg,

339   MD, USA) which have been taken through the whole sample preparation procedure at least during 5

340   separate occasions and measured in total at least 29 times on different days. Uncertainties on mean δ³⁴S

341   per microstructures were calculated by combining individual δ³⁴S measurement uncertainties into one 95%

342   confidence level per microstructure (see **Table 3**).

343

344   **3. Results**

345   3.1 Microscopy

346   Composite reflected light microscopy images (**Fig. 3A-B**; **S1**) show that lenses of chalky microstructure are

347   intercalated between layers of foliated calcite. Under visible light, the chalky microstructure appears opaque

348   and milky white, while the foliated structure is translucent grey. Under higher magnification using SEM, it

349   becomes clear that these differences stem from the microscopic organization of both microstructures:

350   Chalky structures are composed of loosely organized blades of calcite with ample interconnected porosity

351   (**Fig. 3E** and **G**), while the foliated structure consists of densely packed calcite laths organized in semi-

352   parallel bands (**Fig 3D**, **F** and **H**), as observed in Carriker et al. (1980). The proportions of chalky and

353   foliated microstructure differ strongly between specimens (**Fig. 2**). There is no clear consistency in the

354   occurrence of one microstructure over the other in shells of specimens grown in the same environment or

355   in the same growth years (see **Fig. 2**). Mutvei staining (**Fig. 3B**) also allows variations within the foliated

356   microstructure to become visible, highlighting a distinct pattern of dark and light zones ("DZ" and "LZ"

357   respectively) as described for *C. gigas* by Higuera-Ruiz and Elorza (2009).

358   SEM close-ups show that at boundaries on the dorsal (right in **Fig. 3**) side of lenses of chalky structure,

359   where chalky microstructure is precipitated on top of foliated layers, foliated laths change their orientation

360   towards the chalky structure when approaching the boundary, breaking the rigidly organized foliated

361   structure (**Fig 3D** and **G**). On the other side of lenses, where foliated structures are deposited on top of

362   chalky structures, bundles of calcite laths are deposited at a slight angle with respect to the boundary, with

363   some bundles onlapping on (tapering out against) the microstructural boundary (**Fig. 3D** and **H**). Finally,

364   bundles of laths in the foliated structure deposited directly on top of chalky structure are more widely

365   spaced, after which the consecutive bundles gradually regain their typical dense packing (**Fig. 3H**).

366   3.2 Elemental concentrations

367   XRF analysis yielded high-resolution profiles through foliated and chalky microstructures and allowed

368   differences in elemental (Na, Mg, S, Cl, Mn and Sr) composition between the microstructures to be studied

369   in detail (see **Fig. 4** for an example and **S11**, **S3** and **S4** for raw data). Correlation between XRF profiles

370   using color scans and microscopy allowed chalky and foliated calcite that mineralized at the same time to

371   be directly compared. This comparison eliminates environmental or ontogenetic effects, and allows the

372   effect of the microstructure type on shell composition to be studied in isolation. There is a significant ($p <$

373   0.05) difference in the concentrations of Na, Mg, S and Cl between the two microstructures, while Sr and

374   Mn concentrations are not significantly different (**Fig. 5** and **Table 1**). In addition, specimens from the

375   French locality (BR) have significantly higher Sr concentrations than those of the two localities in the

376   Netherlands (TH and MB). Concentrations of Na, Mg, S and Cl in chalky microstructures more closely

377   resemble those of ambient seawater (Pilson, 2012; van Hulten et al. 2016) than those of the foliated

378   microstructure (**S13**).

379
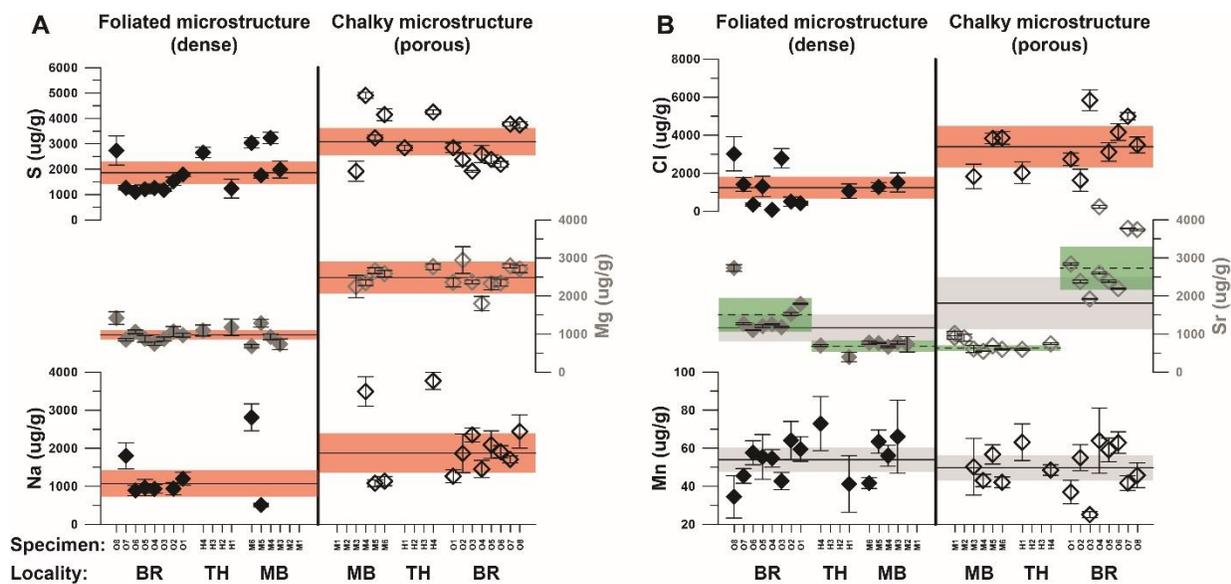
Figure 5: Overview of average concentrations of **A**) Na (black), Mg (grey) and S (black) and **B**) Cl (black), Sr (grey) and Mn (black) in the foliated (closed symbols, left) and chalky (open symbols, right) microstructures. Specimens are grouped by locality: BR = Brittany (specimens **O1-8**), TH = TESO Harbor (Specimens **H1-4**) and MB = Mokbaai (Specimens **M1-6**). Error bars on symbols represent 95 % confidence level estimates on concentrations within specimens. Wide shaded error bars spanning all specimens indicate 95 % confidence levels of inter-specimen variability for the same microstructure. Error bars shaded in red highlight significant ($p < 0.05$) difference between microstructures, while grey error bars indicate no significant difference. The green bars in Sr results highlight significant differences between localities.

Table 1: Summary of elemental concentrations in the foliated and chalky microstructure of C. gigas as measured by µXRF. Uncertainties are reported as 95 % confidence levels and rounded to nearest significant figures (raw data reported in **S13**).

Locality	microstructure	Na (µg/g)		Mg (µg/g)		S (µg/g)		Cl (µg/g)	
TH & MB	chalky	2300	±1700	2500	±1000	3500	±1100	2800	±1600
	foliated	1800	±1100	1040	±350	2380	±740	1580	±930
BR	chalky	1890	±330	2460	±290	2730	±560	3300	±1500
	foliated	1120	±490	980	±170	1510	±440	1240	±920
Combined	chalky	1910	±520	2470	±180	3070	±540	3400	±1100
	foliated	1060	±320	1010	±150	1880	±430	1160	±830

Locality	microstructure	Mn (µg/g)	Sr (µg/g)	Ca (wt %)

TH & MB	chalky	51	±8	628	±71	38.0	±0.8
	foliated	56	±13	680	±150	37.8	±1.2
BR	chalky	49	±11	2730	±560	39.1	±0.1
	foliated	52	±8	1510	±440	39.5	±0.2
Combined	chalky	50	±7	1920	±710	38.6	±0.4
	foliated	54	±6	1150	±340	38.8	±0.7

391

392   3.3 Age model

393   Clear, quasi-sinusoidal variation in Mg concentrations is observed in those XRF profiles which exclusively

394   sample the foliated structure, while these variations are obscured by the alternations between chalky and

395   foliated microstructures in the profiles crossing both microstructures (**Fig. 4**). Sinusoidal variability in Mg

396   concentrations through the foliated calcite is therefore independent of the pattern of microstructural change

397   in the shell hinge. Application of the modified age model reveals that a combination of sinusoids for growth

398   and Mg incorporation (which is assumed to follow seasonality, see **2.5**) can be used to accurately describe

399   this variability in Mg/Ca ratios (Mean R^2 = 0.63; see **S7**; **S13** and **S14**). The modelled growth rate results

400   show that, while growth stops do occur in *C. gigas* in all three localities, these generally have short duration

401   (rarely more than one month) and their timing varies between growth years and between specimens (see

402   **S7** and **S14**). Ages of individuals at the moment of harvest vary between 1.6 and 5.4 years with an average

403   of 3.0 years, with the larger specimens from the Netherlands (TH and MB) being on average older (4.2 ±

404   2.1 years) than French specimens (BR; 2.6 ± 0.7 years; **S11** and **S13**). The age model results also indicate

405   that the growth rate in length direction along the axis of maximum growth is significantly higher in the chalky

406   microstructure (42.0 ± 5.2 µm/d) than in the foliated microstructure (33.0 ± 4.2 µm/d; **S13**).

407   3.4 Elemental distribution coefficients

408   Elemental distribution coefficients (D) were estimated from temporally aligned XRF records of element

409   concentration and seawater concentrations based on high-resolution SSS records (see **2.7**; **Fig. 6**; **Table**

410   **2**; see **S10**). These estimates are independent of seasonal variability in growth rate and SSS, as opposed

411   to estimates of the D from average concentrations of seawater, chalky and foliated calcite, which may be

412   biased if microstructures are over-represented in a specific season or develop preferably under specific

413   conditions. Distribution coefficients of Na, Mg, S and Cl are significantly higher for the chalky microstructure

414 compared to the foliated microstructure ($p < 0.05$). For Mn and Sr, the distribution coefficients of both

415 microstructures are similar. Comparing the estimated D values of Na, Mg, S, Mn and Sr (D_{oyster}) with D

416 values of inorganic calcite (D_{inorg}) from the literature (Kitano et al., 1975; Rimstidt et al., 1998; Day and

417 Henderson, 2013; van Dijk et al., 2017; Hauzer et al., 2018) shows that D_{oyster} of Mg and Mn are significantly

418 lower than D_{inorg} ($p < 0.05$), D_{oyster} of Na and S are higher than D_{inorg}, and D_{oyster} of Sr is statistically similar

419 to D_{inorg}. No D_{inorg} data for Cl were available.
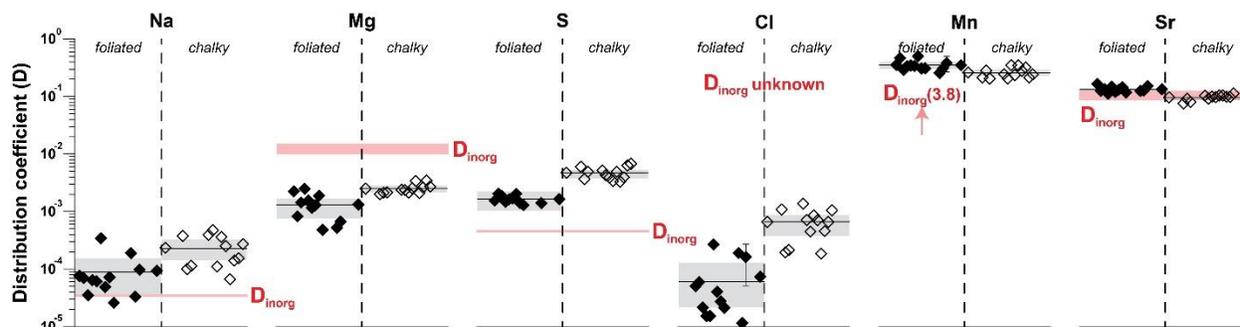
420

421 **Figure 6**: Distribution coefficients (D_{oyster}) of Na, Mg, S, Cl, Mn and Sr for the chalky (open symbols) and

422 foliated (closed symbols) microstructures in C. gigas. Wherever error bars are not shown for individual

423 estimates, the error (95 % confidence level) is within the size of the symbol. Shaded grey bars indicate

424 variability within microstructures, with solid lines indicating the average value for the microstructure. Red

425 bars and numbers indicate literature values for D_{inorg} (Kitano et al., 1975; Rimstidt et al., 1998; Day and

426 Henderson, 2013; van Dijk et al., 2017; Hauzer et al., 2018). Note the logarithmic scale on the vertical axis.

427 **Table 2**: Overview of distribution coefficients (D) of Na, Mg, S, Cl, Mn and Sr between foliated and chalky

428 microstructures and seawater as well as the average SST and SSS under which these microstructures are

429 formed. Note that values for D_{Na}, D_{Mg}, D_S, D_{Cl} and D_{Sr} are multiplied by a factor (behind brackets in column

430 header) for clarity. Uncertainties are given as 95 % confidence levels.

Locality	microstructure	D_{Na} (*10^5)		D_{Mg} (*10^4)		D_S (*10^4)		D_{Cl} (*10^5)	
TH & MB	chalky	25	±12	21.7	±1.3	49.5	±7.0	71	±42
	foliated	8.6	±5.6	5.6	±1.3	13.5	±2.1	9.6	±8.7
BR	chalky	22.8	±6.9	26.6	±2.5	46.0	±4.2	63	±10
	foliated	9.6	±4.0	16.1	±1.9	17.1	±1.1	6.2	±3.6
COMBINED	chalky	23.4	±5.5	25.0	±1.9	47.2	±2.8	66.1	±9.8
	foliated	9.3	±3.0	13.2	±1.6	16.4	±1.1	7.3	±4.3

Locality	microstructure	D_{Mn}		D_{Sr} (*10^3)		SST		SSS	
TH & MB	chalky	0.2	±0.0	87.9	±9.0	12.1	±1.5	28.0	±0.3
	foliated	0.3	±0.1	131	±11	12.2	±2.0	28.1	±0.3
BR	chalky	0.3	±0.0	101.0	±3.2	12.4	±0.6	33.6	±0.2
	foliated	0.4	±0.0	135.2	±5.3	12.0	±0.5	33.5	±0.1
COMBINED	chalky	0.3	±0.0	96.6	±3.1	12.3	±0.6	31.7	±0.5
	foliated	0.4	±0.1	133.8	±4.3	12.1	±0.6	31.7	±0.5

431

432   3.5 Seasonality in microstructures and distribution coefficients

433   Only 15 % of the specimens showed significant annual periodicity in the prevalence of microstructures, and

434   if present this periodicity (seasonality) only explains a small fraction of the variability (adjusted $R^2 \approx 0.50$;

435   **S15**). Similarly, distribution coefficients only exhibit a seasonal component in 29 % of all specimens, which,

436   if present, has limited explaining power (adjusted $R^2 \approx 0.60$). The distribution coefficients of Mg most often

437   exhibit a seasonal component (in 46 % of specimens) and if present the seasonal component in D_{Mg} best

438   fits the data (adjusted $R^2 = 0.75$). This is not surprising, given that age models were based on seasonal

439   variability in Mg/Ca in the shells (see **3.3** and **Fig. 4**) . There is no consistency in the phase of seasonal

440   components in distribution coefficients. Growth rate in the direction of sampling has a strong (adjusted R^2

441   ≈ 0.80) significant seasonal component in 85 % of cases. However, the phase of the seasonality in growth

442   rate is not consistent between specimens. Instead, growth rate in the hinge region of *C. gigas* strongly

443   depends on the local presence of calcite microstructures, which is not seasonally controlled, varies strongly

444   between specimens and is therefore likely not a good measure for growth rates of the entire shell.

445   3.6 Stable isotope values

446   An overview of stable isotope values determined in both microstructures is given in **Fig. 7** and **Table 3**. On

447   average, the two microstructures of *C. gigas* are isotopically highly similar. The only statistically significant

448   ($p < 0.05$) difference between chalky and foliated calcite is observed for $\delta^{18}O_c$ values. In addition, $\delta^{18}O_c$,

449   $\delta^{13}C_c$ and $\delta^{15}N$ values exhibit significant inter-specimen variability. Large variability in $\delta^{18}O_c$ and $\delta^{13}C_c$

450   between and within some specimens is mostly observed in specimens **H1**, **M1** and **M2**, which were

451   microsampled and therefore include seasonal variability (see **S5** and **2.5**), while bulk sampled specimens

452   **M2** and **M6** for combined Δ_{47}, $\delta^{18}O_c$ and $\delta^{13}C_c$ analyses show less internal variability (see **Fig. 7**).

453   Temperatures reconstructed from separate Δ_{47} measurements on foliated and chalky microstructure

454   overestimate the actual mean annual SST by 3.7 °C and 8.4 °C, respectively but fall within the seasonal

455   SST range experienced by the specimens (3-21 °C; see **2.6** and **S13**). This overestimation is not statistically

456   significant in the foliated microstructure (see **Fig. 7** and **S11**). The spread in Δ_{47} is large enough to assume

457   the results from foliated and chalky microstructure to be sampled from the same distribution (Kolmogorov-

458   Smirnov Test: p = 0.03; **S16**). Combining all measurements from both microstructures yields an average

459   temperature of 17.6 ± 2.3°C, which is 6.2 °C warmer than mean annual temperature and the difference with

460   mean annual temperature is statistically significant. Reconstructed $\delta^{18}O_{sw}$ data are not statistically different

461   from those calculated from *in situ* SSS measurements in the environment (-1.56 ± 0.34 ‰VSMOW) and fall

462   within the typical $\delta^{18}O_{sw}$ range reported in previous studies on the Wadden Sea (between -0.8 and -3.3

463   ‰VSMOW for a typical SSS range of 27-33 psu; Witbaard et al., 1994; Böttcher et al., 1998; Harwood et

464   al., 2008). However, foliated calcite yields slightly higher values than the mean annual $\delta^{18}O_{sw}$ (-0.77 ± 0.71

465   ‰VSMOW; equivalent to peak summer values) and chalky structures yield slightly lower $\delta^{18}O_{sw}$ values (-

466   1.83 ± 0.73 ‰VSMOW; closer to winter values; **Fig. 7**; **S8**; **S13**). The foliated calcite exhibited statistically

467   significant inter-specimen differences in $\delta^{15}N$, which are not observed in chalky microstructures. Inter-

468   specimen differences in $\delta^{15}N$ of the foliated microstructure are substantial (inter-specimen standard

469   deviation = 1.19‰) compared to those in the chalky microstructure (SD = 0.21‰) and exceed analytical

470   uncertainty (SD of 0.20‰, see **2.10** and **S11**). Variability in $\delta^{34}S$ between specimens and microstructures

471   is small (<1‰VCTD) and generally smaller than variability within specimens. It can be fully attributed to

472   analytical uncertainty since different aliquots of the same homogenized sample were measured for each

473   specimen and microstructure. As a result, it can be concluded that there is no significant inter-specimen

474   isotopic variability.
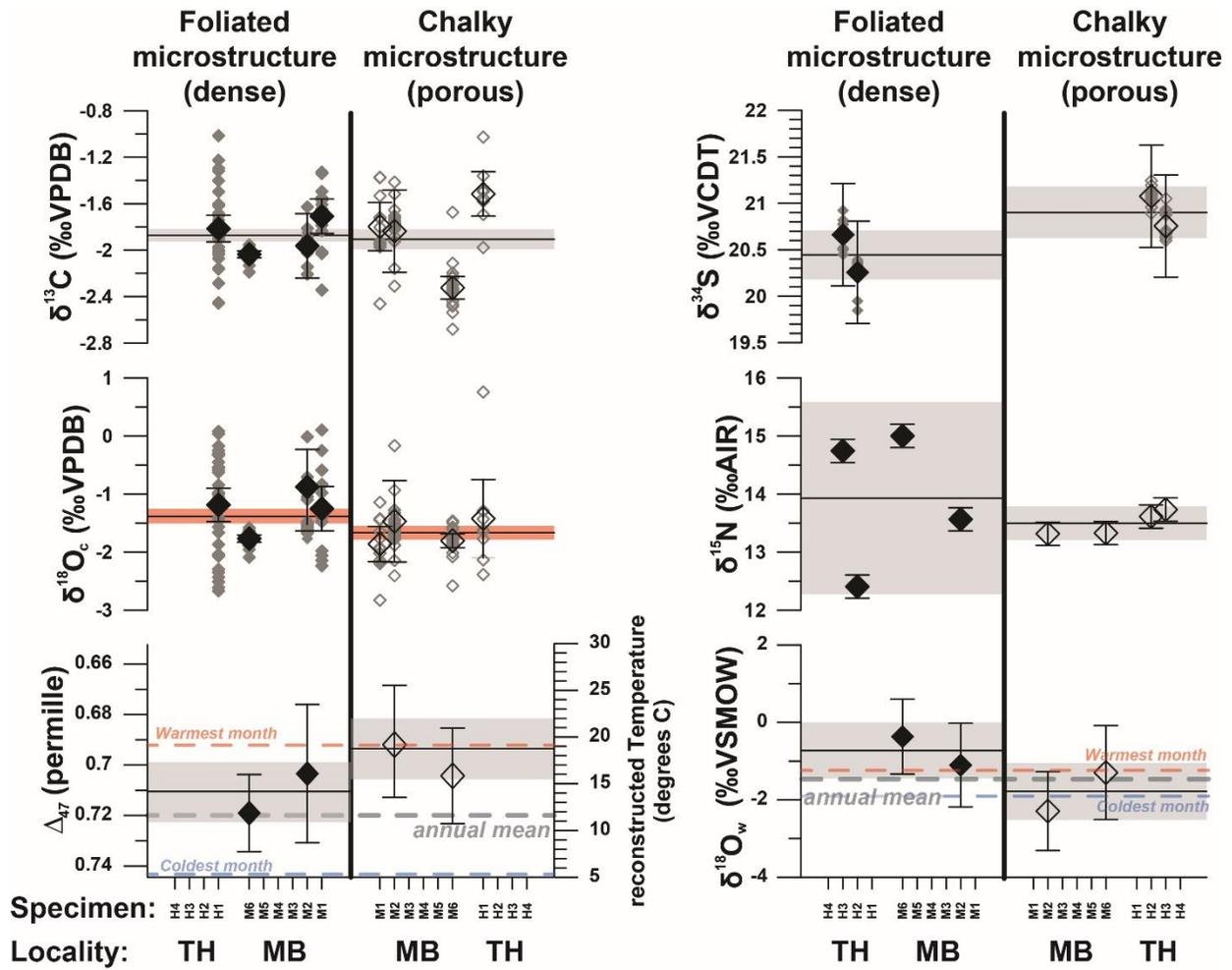
Figure 7: Overview of stable isotope ratio data of foliated (left, closed symbols) and chalky (right, open symbols) microstructures in C. gigas. Color coding of symbols and error bars follows that in **Fig. 5**. Horizontal black, red and blue dashed lines indicate annual mean, summer month and winter month SST and SSS derived from in situ measurements at the NIOZ jetty.

Table 3: Overview of stable isotope ratio data of C. gigas microstructures. Reconstructed sea surface temperatures were calculated from Δ_{47} values and $\delta^{18}O_{sw}$ values were calculated from a combination of SST and $\delta^{18}O_c$. Uncertainties are given as 95 % confidence level.

Microstructure	$\delta^{34}S$ (‰VCDT)		$\delta^{15}N$ (‰AIR)		$\delta^{18}O_c$ (‰VPDB)		$\delta^{13}C_c$ (‰VPDB)	
chalky	20.9	±0.39	13.5	±0.29	-1.67	±0.12	-1.91	±0.09
foliated	20.4	±0.39	13.9	±1.65	-1.39	±0.13	-1.87	±0.05

Microstructure	Δ_{47} (‰)		SST (°C)		$\delta^{18}O_{sw}$ (‰VSMOW)	
chalky	0.706	±0.012	15.9	±3.3	-1.83	±0.73
foliated	0.689	±0.012	20.6	±3.3	-0.77	±0.72

483

4. Discussion

4.1 Timing of microstructural growth

Visible observation and light microscopy images indicate that lenses of chalky microstructure are strictly intercalated between foliated laminae and that they are chronologically separate (i.e. they do not form simultaneously). However, SEM close-ups of boundaries between microstructures (**Fig 3D**, **G** and **H**) show that this is not the case. Transitions of foliated into chalky microstructures consist of gradual changes of orientation of calcite laths instead of sharp boundaries (**Fig. 3D** and **G**). The same is true for the transition from the chalky structure into the foliated structure, as is clear from the truncation of folia in the foliated structure on the boundary between microstructures (**Fig. 3H**). This truncation shows that the lens of chalky structure closes progressively. In the case shown in **Fig. 3H**, precipitation of foliated on top of chalky calcite starts first close to outer margin of the shell hinge and later occurs further away from the outer margin. These observations corroborate detailed structural observations of the microstructures of *C. gigas* by Checa et al. (2018) and demonstrate that foliated and chalky calcite can be deposited simultaneously in different parts of the shell of *C. gigas*. This also explains the lack of consistent seasonality in the occurrence of microstructures (see **3.5** and **S15**). We can therefore conclude that the formation of chalky or foliated microstructure in *Crassostrea gigas* is not linked to the seasonal cycle. However, given the fast growth rate and highly localized nature of chalky lenses both in space and time, a sample of chalky microstructure might nonetheless be easily biased because it was formed predominantly during one season (e.g. summer).

Given the lack of seasonal control, thicker bands of foliated calcite observed in cross-sections through the hinge of this species are likely not reliable as markers for annual growth, as suggested in previous studies (e.g., Harding and Mann, 2006). Similar suggestions for dating other oyster species (e.g., *Ostrea edulis*; Richardson et al., 1993 and *Crassostrea virginica*; Kirby et al., 1998) based on the presence of microstructures should always be backed up with independent evidence such as chemical analysis,

507 especially in fossil specimens (e.g., Kirby et al., 1998; Surge et al., 2001; Harzhauser et al., 2011; Durham

508 et al., 2017; de Winter et al., 2018). Aside from chemical profiles, which may be resource and time-

509 consuming, more reliable estimates for oyster shell age are obtained by chemical labeling (Lartaud et al.,

510 2010a) or counting external growth lines on the resilifer (e.g. Kirby et al., 1998), counting of high-resolution

511 daily and tidal growth increments revealed using cathodoluminescence (Huyghe et al., 2019) or annually-

512 paced dark and light zonation in the foliated microstructure (Higuera-Ruiz et al., 2009). The latter is

513 confirmed by our observations of dark and light zones in foliated calcite (see **Fig. 3**) correlating with

514 seasonal variability in Mg/Ca ratios (see **S7**).

515 4.2 Formation mechanisms of microstructures

516 The lack of seasonality in the expression of microstructure and the strong variability in the timing of the

517 occurrence of microstructures between specimens grown in the same environment (see also **Fig. 2**)

518 suggests that the development of one microstructure over the other is not controlled by environmental

519 factors. Full shell cross-sections (**Fig. 2**; samples **O1-8**) demonstrate that in parts of the shell away from

520 the hinge, the size and frequency of lenses of chalky structure vary also widely within and between

521 specimens. Computer tomography analyses by Banker and Sumner (2020) indicate that lenses of chalky

522 microstructure are local phenomena and their location in three dimensions in the shell depends strongly on

523 the irregular morphology of the shell.

524 While this leaves both the microbial "remote mineralization" hypothesis and the shell plasticity hypothesis

525 for formation of the microstructures open, our stable isotope ratio results strongly favor the shell plasticity

526 hypothesis (**Fig. 8**). The two microstructures are very similar in all isotope systems studied ($\delta^{13}C_c$, $\delta^{15}N$,

527 $\delta^{18}O_c$ and $\delta^{34}S$), with the only significant difference documented in $\delta^{18}O_c$. The latter is forced by strong inter-

528 specimen variability in the microsampled specimens **H1**, **M1** and **M2** due to the large effect of temperature

529 seasonality on $\delta^{18}O_c$ (see **Fig. 7** and **Fig. 8**). Seasonal variability also explains differences in between

530 microstructures within specimens, which are averaged out in intra-specimen means. The sampling bias in

531 **H1**, **M1** and **M2** also causes a small offset in $\delta^{18}O_c$ between microstructures (see also **S13**). If precipitation

532 of the chalky microstructure was mediated by sulphate-reducing bacteria (as suggested in Chinzei and

533 Seilacher, 1993, and Vermeij, 2014), it is expected that the $\delta^{34}S$ value of the resulting carbonate would be

534   much higher (Brunner et al., 2005), resembling those of dissolved sulphate in areas of the modern ocean

535   where bacterial sulphate reduction (BSR) presently takes place (e.g. 'Black Spots' in coastal waters, $\delta^{34}S$

536   = 35-45‰; Böttcher et al., 1998). Instead, the $\delta^{34}S$ composition of both chalky and foliated microstructures

537   in *C. gigas* are not statistically different from that of dissolved sulphate in well-oxygenated North Sea water

538   ($\delta^{34}S$ = 20-21 ‰; Böttcher et al., 2007), oxygenated pore water in surface sediments in the North Sea ($\delta^{34}S$

539   = 20.5-22 ‰; Böttcher et al., 2007) and the carbonate-associated sulphate in other heterotrophic marine

540   calcifiers growing under very similar oxic conditions, and in which no BSR contribution is suspected ($\delta^{34}S$

541   = 21-22 ‰; Richardson et al., 2019). The close agreement between $\delta^{34}S$ in *C. gigas* and dissolved $\delta^{34}S$ in

542   its direct environment shows that both microstructures in oyster shells are reliable recorders of $\delta^{34}S$ of

543   environmental sulphate and, like foraminifera, can be used as archive for changes in $\delta^{34}S$ over geological

544   history (Rennie et al., 2018).

545   Likewise, the similarity of the average $\delta^{15}N$ and $\delta^{13}C_c$ values in the chalky and foliated calcite suggest that

546   in *C. gigas* the two structures are formed by the oyster without pronounced microbial interference. Given

547   the complex interplay of processes that contribute to the N inputs in the North Sea, including river discharge,

548   atmospheric deposition, nutrient consumption and sediment-water fluxes, and their spatial and temporal

549   variability (Rolff et al., 2008, Dähnke et al., 2010), evaluating the isotopic composition of the oyster N source

550   is, at this point, challenging and requires further studies. Our results for oyster-bound $\delta^{15}N$ cluster around

551   13.5 ‰ to 14‰ in the chalky microstructures and around 12.5‰ to 15‰ in the foliated microstructures (**Fig.**

552   **7-8**; **Table 3** and **S11**). These values indicate enrichment in ^{15}N with respect to coastal seawater nitrate,

553   which has been reported to be around 8 – 9 ‰ in the North Sea German Bight, i.e. the closest nitrate $\delta^{15}N$

554   data available (Dähnke et al., 2010). This comparison suggests a 4.5 to 5.5 ‰ enrichment for the oyster

555   with respect to the expected value for exported particulate organic matter, assuming that the available

556   nitrate $\delta^{15}N$ data is representative of that found in our study area. Shell-bound $\delta^{15}N$ is only slightly higher

557   than the value expected after taking into account the 3 - 4 ‰ enrichment per trophic level elevation (DeNiro

558   and Epstein, 1981; Schoeninger & DeNiro, 1984), and suggest that nitrogen is incorporated by the oyster

559   in the two structures without pronounced microbial interference.

560 Carbon isotope ratio values from chalky microstructures ($\delta^{13}C_c$ = -1.91 ± 0.09 ‰VPDB) are

561 indistinguishable from those of the foliated microstructure (-1.87 ± 0.05 ‰VPDB). These values agree more

562 closely with the isotopic composition of dissolved inorganic carbon in well-oxygenated waters (e.g., North

563 Sea; $\delta^{13}C_c$ = -1.5 to 0 ‰VPDB; Salomons and Mook, 1981) than the more depleted values in oxygen-

564 depleted waters (e.g. Baltic Sea floor; $\delta^{13}C_c$ = -4 to 0 ‰VPDB, Voss et al., 2005), where the conditions for

565 BSR are met. Carbon in the shell is likely predominantly derived from DIC and partly by the oyster's diet,

566 with a positive trophic fractionation factor (+2 to 4 ‰; DeNiro and Epstein, 1978; McConnaughey and

567 Gillikin, 2008). Taking this fractionation factor into account, the carbon isotope ratio values measured in *C.*

568 *gigas* microstructures are in even closer agreement with those in well-oxygenated waters, arguing against

569 the hypothesis that conditions allowing BSR to take place prevailed in the extrapallial fluid from which the

570 chalky microstructure formed.

571 The isotopic similarity observed between microstructures provides strong evidence against the "remote

572 mineralization" hypothesis and corroborates findings in previous studies which point towards a common

573 formation pathway for both microstructures (Checa et al., 2019; Banker and Sumner, 2020). In addition,

574 our microscopic observations show smooth microstructural transitions like those described in these

575 previous studies (**Fig. 3**) and a significantly higher growth rate in the chalky microstructure (see **3.3** and

576 **S11**). These observations strengthen the hypothesis that physiological processes such as shell plasticity,

577 growth stress and breakage of the periostracum determine the location and size of pockets of chalky

578 microstructure in the shell of *C. gigas*, and that the chalky structure is an adaptation for oysters to

579 temporarily and locally increase their shell growth rate and produce irregular shells to accommodate

580 irregularities on the surface of their substrate and limited space in their growth environment (Banker and

581 Sumner, 2020). It should be noted that while these findings likely have implications for chalky

582 microstructures observed in related oyster species (e.g. *Crassostrea virginica* or *Ostrea edulis*; Korringa,

583 1951; Carriker et al., 2008), different porous microstructures in other bivalve taxa, such as the vesicular

584 structure in foam oysters (Gryphaeidae; e.g. Stenzel, 1971) may have a different formation pathway which

585 requires independent investigation.
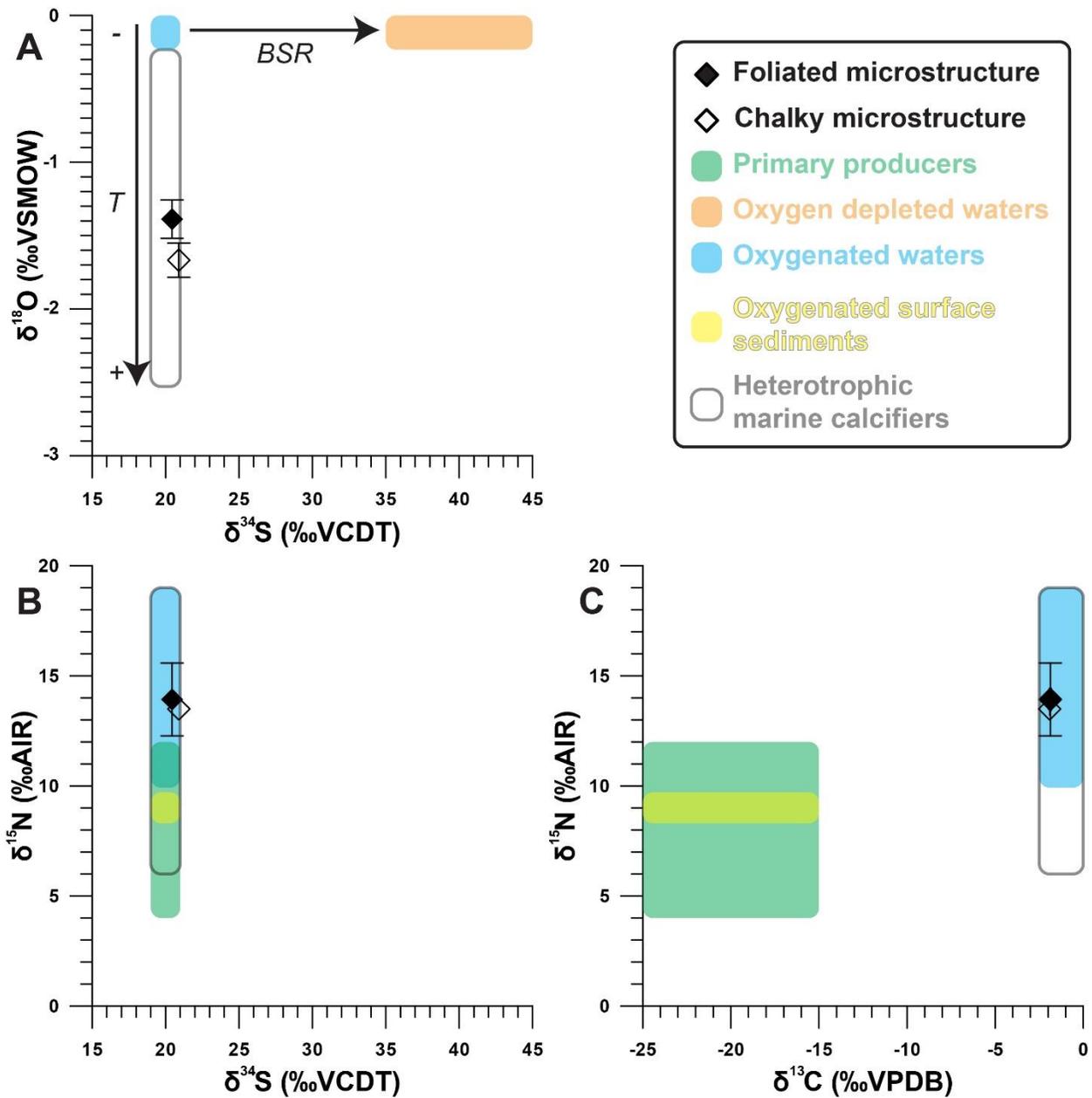
Figure 8: Cross plots of (**A**) $\delta^{18}O_c$ against $\delta^{34}S$, (**B**) $\delta^{15}N$ against $\delta^{34}S$ and (**C**) $\delta^{15}N$ against $\delta^{13}C_c$ showing average stable isotopic compositions of calcite in the foliated (closed symbols) and chalky (open symbols) microstructure of C. gigas compared to the stable isotopic compositions of various compounds in the modern environment taken from the literature: Stable isotope compositions of primary producers from Salomons and Mook, 1981, Stribling and Cornwell, 1997, Pätsch at al., 2010. Stable isotope compositions from oxygen depleted waters from Böttcher et al., 1994, Voss et al., 2005 and Rolff et al., 2008; Bourbonnais et al., 2015. Compositions of well oxygenated waters and oxygenated surface sediments: Salomons and

594 *Mook, 1981, Böttcher et al., 1994 and Pätsch at al., 2010. Compositions of heterotrophic marine calcifiers:*

595 *Ullmann et al., 2013, Gillikin et al., 2017 and Richardson et al., 2019. The black arrow in **A** indicates the*

596 *direction in which Bacterial Sulfate Reduction (BSR) would change the composition of the calcification fluid*

597 *and resulting shell material.*

598 4.3 Trace element partitioning

599 Incorporation of Sr into both microstructures of *C. gigas* is likely close to elemental equilibrium. This is clear

600 from the observation that the distribution coefficient of Sr lacks seasonal variability (see **S15** and time series

601 of D values in **S11**), distribution coefficients of Sr are similar between different microstructures and Sr

602 distribution coefficients in *C. gigas* are similar to those in inorganic calcite (**Fig. 6**). Distribution coefficients

603 of Sr into inorganic aragonite do vary with temperature (Gaetani and Cohen, 2006), but this temperature

604 dependency was not observed in the D_{Sr} of inorganic calcite (Day and Henderson, 2013). Therefore, the

605 lack of seasonality in oyster D_{Sr} does not exclude equilibrium for incorporation of Sr. Differences in Sr

606 concentration between microstructures (see **Fig. 4**; **S14**) likely reflect actual variability in the Sr composition

607 of the extrapallial fluid of the oyster, driven by either environmental variability or physiological changes

608 ("vital effects") unrelated to the environment (e.g. Lorrain et al., 2005; Wanamaker et al., 2008; Schöne et

609 al., 2011; Ullmann et al., 2013). The similarity of D_{Sr} between the microstructures is surprising given the

610 strong influence of calcification rate on the incorporation of Sr into calcite (Lorens, 1981) and the observed

611 difference in growth rate between the microstructures (see **3.3**). It is therefore possible that, while shell

612 extension rate is higher for the chalky structure, the calcification rate (volume of calcite deposited per unit

613 time) is similar owing to the higher porosity of the chalky structure.

614 Differences in the concentrations of Na, Mg, S and Cl between microstructures are unrelated to

615 environmental variability, as is clear from consistency between Na, Mg, S and Cl distribution coefficients of

616 the same microstructure in individuals from different environments (**Fig. 6**) and the lack of seasonal forcing

617 on microstructural expression. Because our data effectively rule out separate biological formation pathways

618 for the microstructures (see **4.2**), significant differences in local shell growth rate (**3.3**) are likely the main

619 driver of variability in elemental concentrations. Compared with inorganic calcite, *C. gigas* discriminates

620 more strictly against the incorporation of Mg and incorporates more Na and S into its shell (**Fig. 6**).

621   Unfortunately, no Cl distribution coefficient between inorganic calcite and water was found in the literature.

622   Interestingly, concentrations of Na, Mg, S and Cl in the chalky structure are always closer to the marine

623   concentrations than those in the foliated structure (i.e., distribution coefficient closer to 1; see **Fig. 6**; **Table**

624   **2**). Na and Cl co-vary on the microscale (**Fig. 4**), but their relative concentrations are not similar to those of

625   sea water. This, together with recent models for oyster shell formation, which leave no possibility of direct

626   exchange between shell porosity and seawater (Banker and Sumner, 2020), seems to rule out the

627   possibility that elemental concentrations in the chalky structure are partly driven by seawater entering the

628   pores in this shell structure.

629   Relationships between growth rate and element uptake into bivalve shell carbonate have been observed in

630   previous studies (e.g. Carré et al., 2006). One possible explanation for this growth rate effect is that during

631   higher growth rates the Ca^{2+}-pump which bivalves use to artificially keep the extrapallial fluid supersaturated

632   with respect to calcium carbonate cannot keep up with the rate of carbonate precipitation. The Ca^{2+}-pump

633   in mollusks adds Ca to the extrapallial fluid, but discriminates actively against other ions, such as Mg and

634   Sr, which may cause impurities in the shell carbonate (Hagiwara and Byerly, 1981; Klein et al., 1996). When

635   fast biomineralization rates exceed the capacity of the Ca^{2+}-pump, Ca and other cations enter the

636   extrapallial fluid through diffusive pathways which do not discriminate against ions other than Ca. Since the

637   concentrations of Na, Mg, S and Cl are high in seawater (Pilson, 2012), these ions will be diffused into the

638   extrapallial fluid at much higher rate than through the Ca^{2+}-pumping pathway. This increases the distribution

639   coefficient of elements with high marine concentrations in fast growing biogenic carbonates (Carré et al.,

640   2006). In addition, crystal growth rate also directly influences element partitioning into carbonates

641   (Busenberg and Niel Plummer, 1985), causing the higher concentrations of elements in the extrapallial fluid

642   to be taken up more readily into shell calcite. This explains why *C. gigas* cannot discriminate against these

643   common ions as effectively in the fast-growing chalky microstructure as compared to the slower growing

644   foliated microstructure.

645   4.4 Implications for oyster shells as archives for environmental change

646   The observation that there is no fundamental difference between the formation pathways of chalky and

647   foliated microstructures in *Crassostrea gigas* indicates that stable isotope ratio analyses of chalky and

648   foliated calcite that grew simultaneously should in theory yield the same result. Since the main difference

649   between the microstructures is their biomineralization rate, isotope data should nevertheless be interpreted

650   with care, as differences in growth rate have been demonstrated to cause kinetic fractionation which may

651   significantly change isotope ratios in fast-growing biominerals (Owen et al., 2002; Bajnai et al., 2018),

652   although this effect is not often observed in bivalves. Within this study, we did not find a significant difference

653   in isotopic composition that can be explained by difference in microstructure. However, differences in

654   average growth rate between chalky (42.0 ± 5.2 μm/d) and foliated microstructure (33.0 ± 4.2 μm/d) are

655   small, so this does not necessarily rule out the influence of kinetic effects. While kinetic effects are known

656   to cause departure from carbonate isotope equilibrium in brachiopods (Bajnai et al., 2018), brachiopods

657   and bivalves have different biomineralization pathways so this result may not apply to *C. gigas*. Instead, a

658   more likely explanation for the difference in Δ_{47}-derived SST reconstructions between the microstructures

659   is a difference in the timing of their formation. Even though bulk sampling for carbonate clumped isotope

660   analyses was carried out to average out seasonal variability, the fast and local mineralization of lenses of

661   chalky calcite may have caused a sampling bias in Δ_{47} samples which explains part of the offset between

662   microstructures. Disproportional summer influence on chalky calcite formation should bias reconstructions

663   from chalky calcite towards higher $\delta^{18}O_{sw}$, because summers are characterized by higher SSS and $\delta^{18}O_{sw}$

664   (see **Fig. 7** and **S8**). In fact, the $\delta^{18}O_{sw}$ reconstructions from chalky calcite are lower than the annual mean,

665   although the difference is not statistically significant and direct comparison of bulk isotopic values with

666   environmental $\delta^{18}O_{sw}$ and SST is complicated by the large seasonal variability in the environment (see **3.6**;

667   **Fig. 7** and **S8**). In absence of strong evidence for kinetic effects, the most likely explanation for the fact that

668   Δ_{47} reconstructions yield temperatures above the annual average is that growth of *C. gigas* is biased

669   towards warmer parts of the year. This bias is clearly stronger in the chalky microstructure. Potential

670   differences between microstructures due to kinetic effects should not be neglected when calibrating proxies

671   for environmental variables in oyster shells, and have also been observed in other bivalve taxa (e.g., *Arctica*

672   *islandica*; Trofimova et al., 2018). However, testing whether these effects play a role in clumped isotope

673   reconstructions requires seasonally resolved Δ_{47} records to be compared to temporally aligned *in situ* SST

674   records, rather than to the annual average, which may not be representative of the calcification temperature

675   due to seasonal bias (see de Winter et al., 2020a). Our results demonstrate that seasonal bias in bulk

676   samples of mollusk shell carbonate can significantly affect the accuracy of mean annual SST

677   reconstructions. Reconstructions based on seasonally resolved proxy records should be preferred over

678   bulk sampling for such reconstructions.

679   Growth rates vary strongly between individuals and the difference in growth rate between microstructures

680   is larger in the samples from Texel (TH and MB) than in those from Brittany (BR; **S11**). Sudden changes in

681   growth rate throughout the shells of oysters are hard to isolate without the use of detailed, sub-annual scale

682   shell chronologies, such as those based on daily and tidal growth increments (e.g., Huyghe et al., 2019).

683   Therefore, chemical records that cross multiple microstructures should be interpreted with care to avoid

684   growth rate-related biases. For this reason, we recommend that such proxies are developed and applied

685   separately for different microstructures. The lack of environmental influence on microstructural

686   development and the fairly limited prevalence of growth cessations (see **3.3** and **S7**) show that sampling

687   the chalky microstructure can be avoided without compromising coverage of a chemical time-series from

688   *C. gigas* shells, thereby limiting the risk of biasing part of the record used for environmental monitoring or

689   reconstructions. This is important in studies of fossil oyster shells given that previous studies have

690   demonstrated that porous microstructures in oysters are more susceptible to diagenetic alteration, which

691   may compromise recovery of the original chemical signature (e.g., de Winter et al., 2018).

692   Differences in elemental concentration between microstructures observed in this and other studies and the

693   lack of consensus between transfer functions for trace element proxies in oyster shells (**Fig. 5** and e.g.,

694   Surge and Lohmann, 2008; Ullmann et al., 2013; Mouchi et al., 2013; Tynan et al., 2017; see also **Fig. 9**)

695   are caused by a difference between elemental distribution coefficients (**Fig. 6**). The fact that differences in

696   elemental incorporation remain even when controlling for environmental variables (see **3.4** and **3.5**) is

697   problematic for the development of trace element proxies in oyster and other bivalve shells. It seems that

698   growth rate has a strong influence on element incorporation, meaning that variability in growth rates may

699   affect the element composition in the shell and interfere with potential environmental signals recorded in

700   these element profiles. This effect is stronger in chalky microstructure, where growth rates are higher and

701   more variable, but we cannot fully exclude a growth rate effect on elemental concentrations in the foliated

702   microstructure. The difference between estimated distribution coefficients and those for inorganic calcite

703   illustrate that *C. gigas* exerts a strong biological control ("vital effect") on incorporation of these elements in

704   its shell.

705   Nevertheless, the strong seasonal variability found in oyster Mg/Ca ratios (e.g. Ullmann et al., 2013; Mouchi

706   et al., 2013; Durham et al., 2017; Bougeois et al., 2018; this study) likely reflects a real imprint of

707   environmental change on shell chemistry, and can therefore be used to reliably link shell growth to the

708   annual cycle (see Durham et al., 2017). This seasonal variability is clear in Mg/Ca profiles through the

709   foliated microstructure, with limited variability in growth rate, but becomes convoluted in profiles through

710   both microstructures (see **Fig. 4**) demonstrating the effect of biomineralization rate. Significant seasonal

711   imprint was also observed in the distribution coefficient of Mg in roughly half of the specimens studied (see

712   **3.5** and **S15**), demonstrating that partitioning of Mg into oyster calcite has a stronger seasonal component

713   than that of the other elements investigated. Despite the seasonal component, correlations between Mg/Ca

714   ratios and SST in specimens in this study are generally weak ($R^2 < 0.20$; **S5**) and become less significant

715   in profiles that include a mix of microstructures. Part of the low explaining power of these correlations may

716   be explained by the effect of higher frequency variability in SST and/or Mg concentrations in the extrapallial

717   fluid on the high resolution μXRF Mg/Ca profiles related to natural or circadian daily and tidal variability (see

718   de Winter et al., 2020b; **S8** and **S9**). This variability becomes more important with increasing growth rate,

719   when higher order variability is more easily resolved in geochemical profiles, which may partly explain the

720   weaker correlations between Mg/Ca and SST in profiles incorporating the fast-growing chalky

721   microstructure. In specimens in which Mg/Ca ratios correlate more strongly ($R^2 > 0.30$) with temperature

722   (**O4**, **O8** and **M6**; see **S5**), the slope of the correlation for foliated calcite resembles relationships found for

723   *C. virginica* (Surge and Lohmann, 2008) and *Saccustrea glomerata* (Tynan et al., 2017), but deviates from

724   the *C. gigas* calibration by Mouchi et al. (2013) which more closely resembles the regression obtained from

725   including the chalky microstructure in this study (**Fig. 9**), even though Mouchi et al. (2013) based their

726   calculations solely on measurements of foliated microstructures, too. This may be explained by the fact that

727   the calibration by Mouchi et al. (2013) was based on juvenile *C. gigas* specimens which exhibited higher

728   growth rates, much like the chalky microstructure.

729   Given these findings in the context of the great variability in growth rate within oyster shells (due to their

730   plasticity, see Banker and Sumner, 2020), between individuals (see **S13**) and between localities (e.g.,

731   Lartaud et al., 2010b), the likelihood that one universal proxy transfer function can be developed linking Na,

732   Mg, S or Mn concentrations to environmental variables seems small, even when only one microstructure

733   (e.g. the foliated calcite only) is included. One potential solution that should be explored is to incorporate

734   local growth or biomineralization rate as a variable in transfer functions of trace element proxies to isolate

735   its effect. Doing so would require the effect of growth rate on the distribution coefficient of elements into the

736   shell to be quantified by growing bivalve species under controlled conditions and manipulating their growth

737   rate.

738   The incorporation of Sr into the shell of *C. gigas* seems to be more independent of growth rate and its

739   estimated distribution coefficient is statistically indistinguishable from that of inorganic calcite. While our

740   results show that distribution coefficients of Sr in *C. gigas* are independent of seasonality, future work

741   should focus on determining whether Sr/Ca ratios hold any promise as environmental proxy in oyster shells.

742   In addition, the effect of changes in calcification rate on the incorporation of these and other elements in

743   the shells of oysters and other mollusks should be further investigated. This study shows that determining

744   elemental distribution coefficients between shell carbonate and seawater is a valuable tool for evaluating

745   the potential for element concentrations in biogenic carbonates to record environmental variability, and to

746   quantify vital effects in trace element proxies.

747
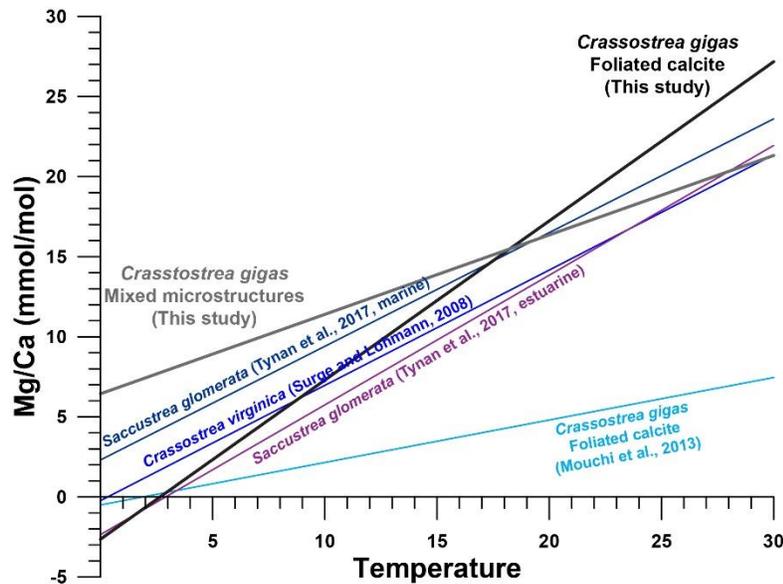
Figure 9: Comparison of regressions between Mg/Ca in oyster shells and temperature. Colored lines show regressions constructed by previous authors. Bold lines show regressions based on data from specimens **O4**, **O8** and **M6** based on measurements in foliated microstructure only (black; $^{Mg}/_{Ca_{shell}} \left[^{mmol}/_{mol} \right] = 0.99 * T[°C] - 2.64$) or lines through both foliated and chalky microstructure (gray; $^{Mg}/_{Ca_{shell}} \left[^{mmol}/_{mol} \right] = 0.50 * T[°C] + 6.44$).

Conclusions

A combination of microscopy, stable isotopic analysis and elemental analysis on 18 specimens of *Crassostrea gigas* from coastal waters in the Netherlands and France reveals that the chalky microstructures in oysters are not formed via microbially assisted carbonate mineralization, which had been proposed previously. Foliated and chalky calcite structures are similar with respect to carbon, nitrogen and sulfur isotope ratios, and show only a minor difference in oxygen isotopic composition. The latter is likely a result of sampling bias given the strong influence of temperature seasonality on the oxygen isotopic compositions in mollusk shells. We observe that clumped isotope analyses on bulk samples of oyster calcite slightly overestimate the mean annual temperature in which the organisms grew, likely due to seasonal sampling bias. The overestimation is significantly smaller for the foliated calcite (+3.7°C) than for the chalky calcite (+8.4°C), probably because the lenses of chalky structure grow locally and during shorter time

764 intervals which increases the risk of seasonal sampling bias. We therefore recommend sampling the foliated

765 over the chalky microstructure for clumped isotope analysis and strongly recommend that seasonality in

766 temperature and growth rate is considered in oyster sclerochronology studies to prevent sampling bias.

767 Detailed shell chronologies show that the presence of microstructures is not linked to environmental

768 changes and that the chalky microstructure can be left unsampled for chemical profiles without introducing

769 hiatuses in the record. Because chalky microstructures in *C. gigas* are characterized by higher and more

770 variable calcification rates, including them may introduce bias in reconstructions and environmental

771 monitoring using proxy records from oyster shells.

772 Elemental distribution coefficients between oyster calcite and seawater show that growth rate has a strong

773 influence on the incorporation of elements into the shell. Of all elements discussed in this study, only

774 strontium seems to be incorporated into the shell of *C. gigas* in equilibrium with sea water. Distribution

775 coefficients of Na, Mg, S, Cl and Mn either differ significantly between the microstructures or deviate

776 significantly from the distribution coefficient for inorganic calcite, suggesting strong biological control on the

777 incorporation of these elements into the shells of oysters. This result shows that there is little promise for

778 the development of universal trace element proxy transfer functions for bivalve shells, unless detailed shell

779 chronologies can be used to correct for changes in calcification rates. Future research should reveal

780 whether the distribution coefficients of elements into the shells of other mollusk species show similar

781 patterns and whether the effect of calcification rates on element incorporation into bivalve shells is universal.

782

801

802   **Supplementary information**

803   All supplementary information is provided in the open-source online repository Zenodo

804   (http://www.doi.org/10.5281/zenodo.3904236)

805

806   **Research Data**

807   Research Data associated with this article can be accessed through the open-source online repository

808   Zenodo at https://doi.org/10.5281/zenodo.3904236.

809

810   **References**

811 Addadi L., Joester D., Nudelman F. and Weiner S. (2006) Mollusk Shell Formation: A Source of New Concepts for Understanding
812   Biomineralization Processes. Chemistry – A European Journal 12, 980–987.

813 Anon (1793) Kungl. Svenska vetenskapsakademiens handlingar.,

814 Bajnai D., Fiebig J., Tomašových A., Milner Garcia S., Rollion-Bard C., Raddatz J., Löffler N., Primo-Ramos C. and Brand U. (2018)
815   Assessing kinetic fractionation in brachiopod calcite using clumped isotopes. Scientific Reports 8, 1–12.

816 Banker R. M. W. and Sumner D. Y. (2020) Structure and distribution of chalky deposits in the Pacific oyster using x-ray computed
817   tomography (CT). Scientific Reports 10, 12118.

818   Boehlke J. K. and Coplen T. B. (1995) Interlaboratory comparison of reference materials for nitrogen-isotope-ratio measurements.,

819   Böttcher M. E., Brumsack H.-J. and Dürselen C.-D. (2007) The isotopic composition of modern seawater sulfate: I. Coastal waters
820   with special regard to the North Sea. Journal of Marine Systems 67, 73–82.

821   Böttcher M. E., Oelschläger B., Höpner T., Brumsack H.-J. and Rullkötter J. (1998) Sulfate reduction related to the early diagenetic
822   degradation of organic matter and "black spot" formation in tidal sandflats of the German Wadden Sea (southern North Sea):
823   stable isotope (13C, 34S, 18O) and other geochemical results. Organic Geochemistry 29, 1517–1530.

824   Bougeois L., Dupont-Nivet G., De Rafélis M., Tindall J. C., Proust J.-N., Reichart G.-J., de Nooijer L. J., Guo Z. and Ormukov C.
825   (2018) Asian monsoons and aridification response to Paleogene sea retreat and Neogene westerly shielding indicated by
826   seasonality in Paratethys oysters. Earth and Planetary Science Letters 485, 99–110.

827   Bourbonnais A., Altabet M. A., Charoenpong C. N., Larkum J., Hu H., Bange H. W. and Stramma L. (2015) N-loss isotope effects in
828   the Peru oxygen minimum zone studied using a mesoscale eddy as a natural tracer experiment. Global Biogeochemical Cycles
829   29, 793–811.

830   Bowen, G.J. (2020) WaterIsotopes.org. Available at: http://wateriso.utah.edu/waterisotopes Accessed July 28, 2020.

831   Braman R. S. and Hendrix S. A. (1989) Nanogram nitrite and nitrate determination in environmental and biological materials by
832   vanadium (III) reduction with chemiluminescence detection. Analytical chemistry 61, 2715–2718.

833   Brunner B., Bernasconi S. M., Kleikemper J. and Schroth M. H. (2005) A model for oxygen and sulfur isotope fractionation in sulfate
834   during bacterial sulfate reduction processes. Geochimica et Cosmochimica Acta 69, 4773–4785.

835   Carré M., Bentaleb I., Bruguier O., Ordinola E., Barrett N. T. and Fontugne M. (2006) Calcification rate influence on trace element
836   concentrations in aragonitic bivalve shells: Evidences and mechanisms. Geochimica et Cosmochimica Acta 70, 4906–4920.

837   Carriker M. R. (1951) Ecological observations on the distribution of oyster larvae in New Jersey estuaries. Ecological Monographs
838   21, 19–38.

839   Carriker M. R., Palmer R. E. and Prezant R. S. (1980) Functional ultramorphology of the dissoconch valves of the oyster
840   Crassostrea virginica. In Proceedings of the National Shellfisheries Association pp. 139–183. Available at:
841   https://www.researchgate.net/profile/Robert_Prezant2/publication/236964411_Functional_ultramorphology_of_the_dissoconch_va
842   lves_of_the_oyster_Crassostrea_virginica/links/53dfd2260cf2a768e49be892.pdf.

843   Checa A. G., Esteban-Delgado F. J. and Rodríguez-Navarro A. B. (2007) Crystallographic structure of the foliated calcite of
844   bivalves. Journal of structural biology 157, 393–402.

845   Checa A. G., Harper E. M. and González-Segura A. (2018) Structure and crystallography of foliated and chalk shell microstructures
846   of the oyster Magallana : the same materials grown under different conditions. Scientific Reports 8, 1–12.

847   Chinzei K. and Seilacher A. (1993) Remote biomineralization I. fill skeletons in vesicular oyster shells. Neues Jahrbuch für Geologie
848   und Paläontologie. Abhandlungen 190, 349–361.

849   Cranford S. and Buehler M. J. (2010) Materiomics: biological protein materials, from nano to macro. Nanotechnology, science and
850   applications 3, 127.

851   Dame R. F. (1999) Oyster reefs as components in estuarine nutrient cycling: Incidental or regulating. Oyster reef habitat restoration:
852   a synopsis and synthesis of approaches. Edited by MW Luckenbach, R. Mann and JA Wesson. Virginia Institute of Marine
853   Science Press, Gloucester Point, 267–280.

854   Dame R. F., Zingmark R. G. and Haskin E. (1984) Oyster reefs as processors of estuarine materials. Journal of Experimental
855   Marine Biology and Ecology 83, 239–247.

856   Day C. C. and Henderson G. M. (2013) Controls on trace-element partitioning in cave-analogue calcite. Geochimica et
857   Cosmochimica Acta 120, 612–627.

858   DeNiro M. J. and Epstein S. (1978) Influence of diet on the distribution of carbon isotopes in animals. Geochimica et cosmochimica
859   acta 42, 495–506.

860   de Winter N. J., Goderis S., Dehairs F., Jagt J. W., Fraaije R. H., Van Malderen S. J., Vanhaecke F. and Claeys P. (2017a) Tropical
861   seasonality in the late Campanian (late Cretaceous): Comparison between multiproxy records from three bivalve taxa from Oman.
862   Palaeogeography, Palaeoclimatology, Palaeoecology 485, 740–760.

863   de Winter N. J., Sinnesael M., Makarona C., Vansteenberge S. and Claeys P. (2017b) Trace element analyses of carbonates using
864   portable and micro-X-ray fluorescence: performance and optimization of measurement parameters and strategies. Journal of
865   Analytical Atomic Spectrometry 32, 1211–1223.

866   de Winter N. J., Vellekoop J., Vorsselmans R., Golreihan A., Soete J., Petersen Sierra. V., Meyer Kyle. W., Casadio S., Speijer
867   Robert. P. and Claeys P. (2018) An assessment of latest Cretaceous Pycnodonte vesicularis (Lamarck, 1806) shells as records
868   for palaeoseasonality: a multi-proxy investigation. Climate of the Past 14, 725–749.

869   de Winter N. J., Ullmann C. V., Sørensen A. M., Thibault N. R., Goderis S., Malderen S. J. M. V., Snoeck C., Goolaerts S.,
870   Vanhaecke F. and Claeys P. (2019) Shell chemistry of the Boreal Campanian bivalve Rastellum diluvianum (Linnaeus, 1767)
871   reveals temperature seasonality, growth rates and life cycle of an extinct Cretaceous oyster. Biogeosciences Discussions, 1–32.

872   de Winter N. J., Müller I. A., Kocken I. J., Thibault N., Ullmann C. V., Farnsworth A., Lunt D. J., Claeys P. and Ziegler M. (2020a)
873   First absolute seasonal temperature estimates for greenhouse climate from clumped isotopes in bivalve shells. *Nature*
874   *Communications* **in review**. Available at: https://www.researchsquare.com/article/rs-39203/v1 [Accessed July 20, 2020].

875   de Winter N. J., Goderis S., Malderen S. J. M. V., Sinnesael M., Vansteenberge S., Snoeck C., Belza J., Vanhaecke F. and Claeys
876   P. (2020b) Subdaily-Scale Chemical Variability in a Torreites Sanchezi Rudist Shell: Implications for Rudist Paleobiology and the
877   Cretaceous Day-Night Cycle. Paleoceanography and Paleoclimatology 35, e2019PA003723.

878   Dähnke K., Emeis K., Johannsen A. and Nagel B. (2010) Stable isotope composition and turnover of nitrate in the German Bight.
879   Marine Ecology Progress Series 408, 7–18.

880   van Dijk I., de Nooijer L. J., Boer W. and Reichart G.-J. (2017) Sulfur in foraminiferal calcite as a potential proxy for seawater
881   carbonate ion concentration. Earth and Planetary Science Letters 470, 64–72.

882   Do Amaral V. S. and Simone L. R. L. (2014) Revision of genus Crassostrea (Bivalvia: Ostreidae) of Brazil. Journal of the Marine
883   Biological Association of the United Kingdom 94, 811–836.

884   Durham S. R., Gillikin D. P., Goodwin D. H. and Dietl G. P. (2017) Rapid determination of oyster lifespans and growth rates using
885   LA-ICP-MS line scans of shell Mg/Ca ratios. Palaeogeography, Palaeoclimatology, Palaeoecology.

886   zu Ermgassen P. S. E., Spalding M. D., Grizzle R. E. and Brumbaugh R. D. (2013) Quantifying the Loss of a Marine Ecosystem
887   Service: Filtration by the Eastern Oyster in US Estuaries. Estuaries and Coasts 36, 36–43.

888   Evans P., Wolff-Briche C. and Fairman B. (2001) High accuracy analysis of low level sulfur in diesel fuel by isotope dilution high
889   resolution ICP-MS, using silicon for mass bias correction of natural isotope ratiosPresented at the 2001 European Winter
890   Conference on Plasma Spectrochemistry, Lillehammer, Norway, February 4–8, 2001. Journal of Analytical Atomic Spectrometry
891   16, 964–969.

892   Fry B., Jannasch H. W., Molyneaux S. J., Wirsen C. O., Muramoto J. A. and King S. (1991) Stable isotope studies of the carbon,
893   nitrogen and sulfur cycles in the Black Sea and the Cariaco Trench. Deep Sea Research Part A. Oceanographic Research Papers
894   38, S1003–S1019.

895   Gillikin D. P., Lorrain A., Jolivet A., Kelemen Z., Chauvaud L. and Bouillon S. (2017) High-resolution nitrogen stable isotope
896   sclerochronology of bivalve shell carbonate-bound organics. Geochimica et Cosmochimica Acta 200, 55–66.

897   Goodwin D. H., Paul P. and Wissink C. L. (2009) MoGroFunGen: A numerical model for reconstructing intra-annual growth rates of
898   bivalve molluscs. Palaeogeography, Palaeoclimatology, Palaeoecology 276, 47–55.

899   Goodwin D. H., Schöne B. R. and Dettman D. L. (2003) Resolution and fidelity of oxygen isotopes as paleotemperature proxies in
900   bivalve mollusk shells: models and observations. Palaios 18, 110–125.

901   Grabowski J. H., Brumbaugh R. D., Conrad R. F., Keeler A. G., Opaluch J. J., Peterson C. H., Piehler M. F., Powers S. P. and
902   Smyth A. R. (2012) Economic valuation of ecosystem services provided by oyster reefs. Bioscience 62, 900–909.

903   Grabowski J. H. and Peterson C. H. (2007) Restoring oyster reefs to recover ecosystem services. Ecosystem engineers: plants to
904   protists 4, 281–298.

905   Gray J. E. (1833) Some observations on the economy of molluscous animals, and the structure of their shells. Philosophical
906   Transactions of the Royal Society of London 123, 771–819.

907   Hagiwara S. and Byerly L. (1981) Calcium channel. Annual review of neuroscience 4, 69–125.

908   Harding J. M. and Mann R. (2006) Age and growth of wild suminoe (Crassostrea ariakensis, Fugita 1913) and Pacific (C. Gigas,
909   Thunberg 1793) oysters from Laizhou bay, China. Journal of Shellfish Research 25, 73–82.

910   Harwood A. J. P., Dennis P. F., Marca A. D., Pilling G. M. and Millner R. S. (2008) The oxygen isotope composition of water masses
911   within the North Sea. *Estuarine, Coastal and Shelf Science* **78**, 353–359.

912   Harzhauser M., Piller W. E., Müllegger S., Grunert P. and Micheels A. (2011) Changing seasonality patterns in Central Europe from
913   Miocene Climate Optimum to Miocene Climate Transition deduced from the Crassostrea isotope archive. Global and Planetary
914   Change 76, 77–84.

915   Hauzer H., Evans D., Müller W., Rosenthal Y. and Erez J. (2018a) Calibration of Na partitioning in the calcitic foraminifer Operculina
916   ammonoides under variable Ca concentration: Toward reconstructing past seawater composition. Earth and Planetary Science
917   Letters 497, 80–91.

918   Hauzer H., Evans D., Müller W., Rosenthal Y. and Erez J. (2018b) Calibration of Na partitioning in the calcitic foraminifer Operculina
919   ammonoides under variable Ca concentration: Toward reconstructing past seawater composition. Earth and Planetary Science
920   Letters 497, 80–91.

921   Higuera-Ruiz R. and Elorza J. (2009) Biometric, microstructural, and high-resolution trace element studies in Crassostrea gigas of
922   Cantabria (Bay of Biscay, Spain): Anthropogenic and seasonal influences. Estuarine, Coastal and Shelf Science 82, 201–213.

923   Höche N., Peharda M., Walliser E. O. and Schöne B. R. (2020) Morphological variations of crossed-lamellar ultrastructures of
924   Glycymeris bimaculata (Bivalvia) serve as a marine temperature proxy. Estuarine, Coastal and Shelf Science 237, 106658.

925 van Hulten M. M. P., Middag R., Dutay J.-C., de Baar H. J. W., Roy-Barman M., Gehlen M., Tagliabue A. and Sterl A. (2016)
926   Manganese in the West Atlantic Ocean in context of the first global ocean circulation model of manganese. arXiv preprint
927   arXiv:1606.07128.

928 Huyghe D., de Rafélis M., Ropert M., Mouchi V., Emmanuel L., Renard M. and Lartaud F. (2019) New insights into oyster high-
929   resolution hinge growth patterns. Marine biology 166, 48.

930 IAEA/WMO, 2015 Global Network of Isotopes in Precipitation. The GNIP Database. Accessible at: https://nucleus.iaea.org/wiser.
931   Accessed: July 28, 2020.

932 Jia L., Cai C., Yang H., Li H., Wang T., Zhang B., Jiang L. and Tao X. (2015) Thermochemical and bacterial sulfate reduction in the
933   C ambrian and L ower O rdovician carbonates in the T azhong A rea, T arim B asin, NW C hina: evidence from fluid inclusions, C,
934   S, and S r isotopic data. Geofluids 15, 421–437.

935 Jones D. S. (1983) Sclerochronology: reading the record of the molluscan shell: annual growth increments in the shells of bivalve
936   molluscs record marine climatic changes and reveal surprising longevity. American Scientist 71, 384–391.

937 Judd E. J., Wilkinson B. H. and Ivany L. C. (2017) The life and time of clams: Derivation of intra-annual growth rates from high-
938   resolution oxygen isotope profiles. Palaeogeography, Palaeoclimatology, Palaeoecology. Available at:
939   http://www.sciencedirect.com/science/article/pii/S0031018217307691.

940 Kennedy V. S., Newell R. I. and Eble A. F. (1996) The eastern oyster: Crassostrea virginica., University of Maryland Sea Grant
941   College.

942 Kirby M. X., Soniat T. M. and Spero H. J. (1998) Stable isotope sclerochronology of Pleistocene and Recent oyster shells
943   (Crassostrea virginica). Palaios 13, 560–569.

944 Kitano Y., Okumura M. and Idogaki M. (1975) Incorporation of sodium, chloride and sulfate with calcium carbonate. Geochemical
945   Journal 9, 75–84.

946 Klein R. T., Lohmann K. C. and Thayer C. W. (1996) SrCa and 13C12C ratios in skeletal calcite of Mytilus trossulus: Covariation
947   with metabolic rate, salinity, and carbon isotopic composition of seawater. Geochimica et Cosmochimica Acta 60, 4207–4221.

948 Korringa P. (1951) On the nature and function of "chalky" deposits in the shell of Ostrea edulis Linnaeus. Proc. Calif. Acad. Sci 27,
949   133–158.

950 Lartaud F., De Rafélis M., Ropert M., Emmanuel L., Geairon P. and Renard M. (2010a) Mn labelling of living oysters: artificial and
951   natural cathodoluminescence analyses as a tool for age and growth rate determination of C. gigas (Thunberg, 1793) shells.
952   Aquaculture 300, 206–217.

953 Lartaud F., Emmanuel L., De Rafélis M., Ropert M., Labourdette N., Richardson C. A. and Renard M. (2010b) A latitudinal gradient
954   of seasonal temperature variation recorded in oyster shells from the coastal waters of France and The Netherlands. Facies 56, 13.

955 Lee S.-W., Jang Y.-N., Ryu K.-W., Chae S.-C., Lee Y.-H. and Jeon C.-W. (2011) Mechanical characteristics and morphological
956   effect of complex crossed structure in biomaterials: fracture mechanics and microstructure of chalky layer in oyster shell. Micron
957   42, 60–70.

958 Lorrain A., Gillikin D. P., Paulet Y.-M., Chauvaud L., Le Mercier A., Navez J. and André L. (2005) Strong kinetic effects on Sr/Ca
959   ratios in the calcitic bivalve Pecten maximus. Geology 33, 965–968.

960 Lueders-Dumont J. A., Wang X. T., Jensen O. P., Sigman D. M. and Ward B. B. (2018) Nitrogen isotopic analysis of carbonate-
961   bound organic matter in modern and fossil fish otoliths. Geochimica et Cosmochimica Acta 224, 200–222.

962 Luz G. M. and Mano J. F. (2010) Mineralized structures in nature: Examples and inspirations for the design of new composite
963   materials and biomaterials. Composites Science and Technology 70, 1777–1788.

964 McConnaughey T. A. and Gillikin D. P. (2008) Carbon isotopes in mollusk shell carbonates. Geo-Marine Letters 28, 287–299.

965 McGenity T. J. and Sellwood B. W. (1999) New approaches to studying the microbial precipitation of carbonate minerals.
966   Sedimentary geology 126, 5–8.

967 Mehra O. P. and Jackson M. L. (2013) Iron oxide removal from soils and clays by a dithionite–citrate system buffered with sodium
968   bicarbonate. In Clays and clay minerals Elsevier. pp. 317–327.

969 Mook W. G. (1970) Stable carbon and oxygen isotopes of natural waters in the Netherlands. Isotope hydrology 1970, 163–190.

970 Mouchi V., De Rafélis M., Lartaud F., Fialin M. and Verrecchia E. (2013) Chemical labelling of oyster shells used for time-calibrated
971   high-resolution Mg/Ca ratios: a tool for estimation of past seasonal temperature variations. Palaeogeography, Palaeoclimatology,
972   Palaeoecology 373, 66–74.

973 Newell R. I. (1988) Ecological changes in Chesapeake Bay: are they the result of overharvesting the American oyster, Crassostrea
974   virginica. Understanding the estuary: advances in Chesapeake Bay research 129, 536–546.

975 Nydahl F. (1978) On the peroxodisulphate oxidation of total nitrogen in waters to nitrate. Water Research 12, 1123–1130.

976 Owen R., Kennedy H. and Richardson C. (2002) Isotopic partitioning between scallop shell calcite and seawater: effect of shell
977   growth rate. Geochimica et Cosmochimica Acta 66, 1727–1737.

978 Paris G., Sessions A. L., Subhas A. V. and Adkins J. F. (2013) MC-ICP-MS measurement of δ34S and ∆33S in small amounts of
979   dissolved sulfate. Chemical Geology 345, 50–61.

980 Pilson M. E. (2012) An Introduction to the Chemistry of the Sea., cambridge university press.

981 Pracht H., Metcalfe B. and Peeters F. J. C. (2018) Oxygen isotope composition of final chamber of planktic foraminifera provides
982   evidence for vertical migration and depth integrated growth., Paleobiogeoscience: Proxy use, Development & Validation.
983   Available at: https://www.biogeosciences-discuss.net/bg-2018-146/bg-2018-146.pdf [Accessed June 9, 2020].

984 Qi H., Coplen T. B., Geilmann H., Brand W. A. and Böhlke J. K. (2003) Two new organic reference materials for δ13C and δ15N
985   measurements and a new value for the δ13C of NBS 22 oil. Rapid Communications in Mass Spectrometry 17, 2483–2487.

986 Ren H., Sigman D. M., Meckler A. N., Plessen B., Robinson R. S., Rosenthal Y. and Haug G. H. (2009) Foraminiferal isotope
987   evidence of reduced nitrogen fixation in the ice age Atlantic Ocean. Science 323, 244–248.

988 Rennie V. C., Paris G., Sessions A. L., Abramovich S., Turchyn A. V. and Adkins J. F. (2018) Cenozoic record of δ 34 S in
989   foraminiferal calcite implies an early Eocene shift to deep-ocean sulfide burial. Nature Geoscience 11, 761–765.

990 Richardson C. A., Collis S. A., Ekaratne K., Dare P. and Key D. (1993) The age determination and growth rate of the European flat
991   oyster, Ostrea edulis, in British waters determined from acetate peels of umbo growth lines. ICES Journal of Marine Science 50,
992   493–500.

993 Richardson J. A., Newville M., Lanzirotti A., Webb S. M., Rose C. V., Catalano J. G. and Fike D. A. (2019a) The source of sulfate in
994   brachiopod calcite: Insights from μ-XRF imaging and XANES spectroscopy. Chemical Geology 529, 119328.

995 Richardson J. A., Newville M., Lanzirotti A., Webb S. M., Rose C. V., Catalano J. G. and Fike D. A. (2019b) The source of sulfate in
996   brachiopod calcite: Insights from μ-XRF imaging and XANES spectroscopy. Chemical Geology 529, 119328.

997 Rimstidt J. D., Balog A. and Webb J. (1998) Distribution of trace elements between carbonate minerals and aqueous solutions.
998   Geochimica et Cosmochimica Acta 62, 1851–1863.

999 Rolff C., Elmgren R. and Voss M. (2008) Deposition of nitrogen and phosphorus on the Baltic Sea: seasonal patterns and nitrogen
1000   isotope composition. Biogeosciences Discussions 5.

1001 Salomons W. and Mook W. G. (1981) Field observations of the isotopic composition of particulate organic carbon in the southern
1002   North Sea and adjacent estuaries. Marine Geology 41, M11–M20.

1003 Salvi D., Macali A. and Mariottini P. (2014) Molecular phylogenetics and systematics of the bivalve family Ostreidae based on rRNA
1004   sequence-structure models and multilocus species tree. PLoS One 9, e108696.

1005 Schimmelmann A., Qi H., Coplen T. B., Brand W. A., Fong J., Meier-Augenstein W., Kemp H. F., Toman B., Ackermann A. and
1006   Assonov S. (2016) Organic reference materials for hydrogen, carbon, and nitrogen stable isotope-ratio measurements: caffeines,
1007   n-alkanes, fatty acid methyl esters, glycines, L-valines, polyethylenes, and oils. Analytical chemistry 88, 4294–4302.

1008 Schindelin J., Arganda-Carreras I., Frise E., Kaynig V., Longair M., Pietzsch T., Preibisch S., Rueden C., Saalfeld S. and Schmid B.
1009   (2012) Fiji: an open-source platform for biological-image analysis. Nature methods 9, 676–682.

1010 Schoeninger M. J. and DeNiro M. J. (1984) Nitrogen and carbon isotopic composition of bone collagen from marine and terrestrial
1011   animals. Geochimica et Cosmochimica acta 48, 625–639.

1012 Schöne B. R., Dunca E., Fiebig J. and Pfeiffer M. (2005a) Mutvei's solution: An ideal agent for resolving microgrowth structures of
1013   biogenic carbonates. Palaeogeography, Palaeoclimatology, Palaeoecology 228, 149–166.

1014 Schöne B. R., Houk S. D., Castro A. D. F., Fiebig J., Oschmann W., Kröncke I., Dreyer W. and Gosselck F. (2005b) Daily growth
1015   rates in shells of Arctica islandica: assessing sub-seasonal environmental controls on a long-lived bivalve mollusk. Palaios 20, 78–
1016   92.

1017 Schöne B. R., Zhang Z., Radermacher P., Thébault J., Jacob D. E., Nunn E. V. and Maurer A.-F. (2011) Sr/Ca and Mg/Ca ratios of
1018   ontogenetically old, long-lived bivalve shells (Arctica islandica) and their function as paleotemperature proxies. Palaeogeography,
1019   Palaeoclimatology, Palaeoecology 302, 52–64.

1020 Scyphers S. B., Powers S. P., Heck Jr K. L. and Byron D. (2011) Oyster reefs as natural breakwaters mitigate shoreline loss and
1021   facilitate fisheries. PloS one 6.

1022 Sigman D. M., Casciotti K. L., Andreani M., Barford C., Galanter M. and Böhlke J. K. (2001) A bacterial method for the nitrogen
1023   isotopic analysis of nitrate in seawater and freshwater. Analytical chemistry 73, 4145–4153.

1024 Straub M., Sigman D. M., Ren H., Martínez-García A., Meckler A. N., Hain M. P. and Haug G. H. (2013) Changes in North Atlantic
1025   nitrogen fixation controlled by ocean circulation. Nature 501, 200–203.

1026 Stenzel H. B. (1971) Oysters. Treatise on Invertebrate Paleontology, Part N, Bivalvia 3, N953–N1224.

1027 Stribling J. M. and Cornwell J. C. (1997) Identification of important primary producers in a Chesapeake Bay tidal creek system using
1028   stable isotopes of carbon and sulfur. Estuaries 20, 77–85.

1029 Surge D. and Lohmann K. C. (2008) Evaluating Mg/Ca ratios as a temperature proxy in the estuarine oyster, Crassostrea virginica.
1030   J. Geophys. Res. 113, G02001.

1031 Surge D., Lohmann K. C. and Dettman D. L. (2001a) Controls on isotopic chemistry of the American oyster, Crassostrea virginica:
1032   implications for growth patterns. Palaeogeography, Palaeoclimatology, Palaeoecology 172, 283–296.

1033 Surge D., Lohmann K. C. and Dettman D. L. (2001b) Controls on isotopic chemistry of the American oyster, Crassostrea virginica:
1034   implications for growth patterns. Palaeogeography, Palaeoclimatology, Palaeoecology 172, 283–296.

1035 Surge Donna, Lohmann K. C. and Dettman D. L. (2001) Controls on isotopic chemistry of the American oyster, Crassostrea
1036   virginica: implications for growth patterns. Palaeogeography, Palaeoclimatology, Palaeoecology 172, 283–296.

1037 Terakado Y., Ofuka Y. and Tada N. (2010) Rare earth elements, Sr, Ba, Fe, and major cation concentrations in some living
1038   foraminiferal tests collected from Iriomote Island, Japan: An exploration for trace element behavior during biogenic calcium
1039   carbonate formation. Geochemical Journal 44, 315–322.

1040 THUNBERG C. (1793) Teckning och beskrifning pa en stor Ostronsort ifran Japan. K. Svenska Vetenskapsakademien, Handlinger.

1041 Tynan S., Opdyke B. N., Walczak M., Eggins S. and Dutton A. (2017) Assessment of Mg/Ca in Saccostrea glomerata (the Sydney
1042   rock oyster) shell as a potential temperature record. Palaeogeography, palaeoclimatology, palaeoecology 484, 79–88.

1043 Ullmann C. V., Böhm F., Rickaby R. E. M., Wiechert U. and Korte C. (2013) The Giant Pacific Oyster (Crassostrea gigas) as a
1044   modern analog for fossil ostreoids: Isotopic (Ca, O, C) and elemental (Mg/Ca, Sr/Ca, Mn/Ca) proxies. Geochem. Geophys.
1045   Geosyst. 14, 4109–4120.

1046 Ullmann C. V., Wiechert U. and Korte C. (2010) Oxygen isotope fluctuations in a modern North Sea oyster (Crassostrea gigas)
1047   compared with annual variations in seawater temperature: Implications for palaeoclimate studies. Chemical Geology 277, 160–
1048   166.

1049 Vermeij G. J. (2014) The oyster enigma variations: a hypothesis of microbial calcification. Paleobiology 40, 1–13.

1050 Voss M., Liskow I., Pastuszak M., Rüß D., Schulte U. and Dippner J. W. (2005) Riverine discharge into a coastal bay: A stable
1051   isotope study in the Gulf of Gdańsk, Baltic Sea. Journal of Marine Systems 57, 127–145.

1052 Wanamaker Jr A. D., Kreutz K. J., Wilson T., Borns Jr H. W., Introne D. S. and Feindel S. (2008) Experimentally determined Mg/Ca
1053   and Sr/Ca ratios in juvenile bivalve calcite for Mytilus edulis: implications for paleotemperature reconstructions. Geo-Marine
1054   Letters 28, 359–368.

1055 Wang X. T., Prokopenko M. G., Sigman D. M., Adkins J. F., Robinson L. F., Ren H., Oleynik S., Williams B. and Haug G. H. (2014)
1056   Isotopic composition of carbonate-bound organic nitrogen in deep-sea scleractinian corals: A new window into past
1057   biogeochemical change. Earth and Planetary Science Letters 400, 243–250.

1058 Wang X. T., Sigman D. M., Cohen A. L., Sinclair D. J., Sherrell R. M., Cobb K. M., Erler D. V., Stolarski J., Kitahara M. V. and Ren
1059   H. (2016) Influence of open ocean nitrogen supply on the skeletal $\delta^{15}N$ of modern shallow-water scleractinian corals. Earth and
1060   Planetary Science Letters 441, 125–132.

1061 Webb G. E. and Kamber B. S. (2000) Rare earth elements in Holocene reefal microbialites: a new shallow seawater proxy.
1062   Geochimica et Cosmochimica Acta 64, 1557–1565.

1063 Weigand M. A., Foriel J., Barnett B., Oleynik S. and Sigman D. M. (2016) Updates to instrumentation and protocols for isotopic
1064   analysis of nitrate by the denitrifier method. Rapid Communications in Mass Spectrometry 30, 1365–1383.

1065 Wilkinson B. H. and Ivany L. C. (2002) Paleoclimatic inference from stable isotope profiles of accretionary biogenic hardparts – a
1066   quantitative approach to the evaluation of incomplete data. Palaeogeography, Palaeoclimatology, Palaeoecology 185, 95–114.

1067 Witbaard R., Jenness M. I., Van Der Borg K. and Ganssen G. (1994) Verification of annual growth increments in Arctica islandica L.
1068   from the North Sea by means of oxygen and carbon isotopes. *Netherlands Journal of Sea Research* **33**, 91–101.

1069 Yonge C. M. (1960) The New Naturalist Special Volume-Oysters.